https://doi.org/10.5194/egusphere-2026-4309
Preprint. Discussion started: 17 August 2026

First Assessment of SWOT KaRIn Measurements Over Lake Ice and Overlying Snow

Jaya Sree Mugunthan[1], Claude R. Duguay[1,2,3], Justin Murfitt[1], Elena Zakharova[4], Benjamin M. Jones[5]

[1]H2O Geomatics, Waterloo, N2L 6R5, Canada
[2]Hydro-EO, Salir do Porto, 2500-673, Portugal
[3]University of Waterloo, Waterloo, N2L 3G1, Canada
[4]EOLA, Toulouse, France
[5]Institute of Northern Engineering, University of Alaska Fairbanks, Fairbanks, 99775-5910, USA

Correspondence to: Jaya Sree Mugunthan (jayasree.mugunthan@h2ogeomatics.com)

Abstract. The Surface Water and Ocean Topography (SWOT) mission, launched on December 16, 2022, carries a Ka-band Radar Interferometer (KaRIn) and provides high-resolution, wide-swath measurements of Earth's surface waters. During the Cal/Val phase (March 29 to July 09, 2023; local date), near-daily observations were acquired over Teshekpuk Lake, Alaska, providing an opportunity to examine the response of KaRIn measurements to lake ice and overlying snow conditions. Using optical and SAR imagery, reanalysis products, and field observations during the same period, we found that SWOT heights provide reasonable elevations over the fully ice-covered (before melt onset) and open water surfaces. Meanwhile, Ka-band backscatter effectively tracks the evolution of snow conditions, freeze/melt events, surface melt onset, and ice break-up, as well as features such as pressure ridges, the inlet stream, cracks, and fragmented ice. Limitations were also found in the SWOT Level 2 KaRIn High-Rate Pixel Cloud Version D data used, particularly in the quality of height retrievals over melting ice, in areas contaminated by specular ringing, and on surfaces with little to no wind. Complementary simulations with the Snow Microwave Radiative Transfer (SMRT) model confirmed the sensitivity of Ka-band backscatter to evolving snow properties (snow density and grain size). These results highlight SWOT's ability to advance the monitoring of ice-covered lakes and their seasonal dynamics, and to support the development of retrieval algorithms of ice and overlying snow properties in preparation for the launch of future satellite missions providing Ka-band frequency measurements, such as the Copernicus polaR Ice and Snow Topography ALtimeter (CRISTAL) and Sentinel-3 Next Generation Topography (S3NG-TOPO) missions.

Keywords: SWOT, lake ice, snow, interferometry, swath altimetry

https://doi.org/10.5194/egusphere-2026-4309
Preprint. Discussion started: 17 August 2026

1 Introduction

High-latitude lakes experience seasonal ice formation due to prolonged periods of sub-freezing temperatures, characteristic of boreal and Arctic environments. Given the abundance and broad spatial distribution of lakes across the Northern Hemisphere, lake ice represents an important part of the cryosphere (Brown & Duguay, 2010; Prowse et al., 2011; Verpoorter et al., 2014; Messager et al., 2016). Ice formation on these lakes begins in late fall/early winter and progresses through winter as the ice thickens. With the arrival of warmer spring temperatures, the ice gradually melts, ultimately leading to an ice-free state. This seasonal cycle of lake ice cover, from ice formation to complete ice-free conditions, is called lake ice phenology. Lake ice may also experience intermittent melting and refreezing episodes, influenced by transient weather conditions. The timing of freeze/melt, ice growth, and the duration of ice cover depend on various factors, such as air temperature, snow accumulation, wind conditions, and lake morphometry (Jeffries et al., 2005; Brown & Duguay, 2010; Duguay et al., 2015). To acknowledge lakes' importance and sensitivity to climate change, the Global Climate Observation System (GCOS) identifies lake ice cover (LIC) and lake ice thickness (LIT) as two thematic variables of Lakes as an Essential Climate Variable (ECV) (Zemp et al., 2022).

Despite their climatic and hydrological importance, high-latitude lakes are significantly under-monitored due to logistical challenges in in situ data collection (Murfitt & Duguay, 2021). Given the decline in ground-based monitoring of lake ice, there has been growing reliance on satellite-based remote sensing, which provides consistent, global observations of lakes at medium to high spatial and temporal resolutions (Duguay et al., 2015). Over the past few decades, both optical (e.g., MODIS, Landsat, Sentinel-2) and microwave (e.g., AMSR-E, Sentinel-1, Jason) sensors have been widely employed to monitor lake ice phenology, assess freeze-thaw dynamics, and detect trends. Optical remote sensing systems are most frequently used for mapping/monitoring lake ice cover extent and ice phenology (Arp et al., 2013; Murfitt & Brown, 2017; Liu et al., 2021; Wang et al., 2021). However, they are fundamentally limited by their dependence on solar illumination. Persistent cloud cover, common in polar and boreal regions, along with prolonged winter darkness, significantly reduces their usability for ice phenology. On the other hand, microwave remote sensing systems can penetrate clouds and operate under all-weather and day-night conditions, making them particularly effective in high-latitude settings where optical methods struggle. Satellite radar altimeters, a type of active microwave system, have been successfully used in hydrology and cryosphere applications for the past few decades. Unlike optical or radar imagery, altimeters provide a linear profile of surface elevation directly beneath the satellite path (nadir observations), as they record the signals sent from the satellite and reflected back from the Earth's surface. Altimetry complements the information obtained from optical and SAR imaging systems by providing measurements of surface elevation, including water level and, via suitable retrieval schemes, ice thickness, as well as surface-type information (Kouraev et al., 2007; Atwood et al., 2015; Gunn et al., 2017; Murfitt & Duguay, 2020; Mugunthan et al., 2023; Mangilli et al., 2024).

https://doi.org/10.5194/egusphere-2026-4309
Preprint. Discussion started: 17 August 2026

The launch of the Surface Water and Ocean Topography (SWOT) mission on December 16, 2022, takes satellite altimetry to a new level, as it is the first satellite to provide surface elevation in a two-dimensional format. This swath altimeter overcomes many limitations of traditional pulse-limited and Synthetic Aperture Radar (SAR) altimeters, including limited spatial coverage from narrow nadir profiles and lower resolution from larger footprints. Hence, with SWOT, it is possible to obtain both the target extent and elevation information at high resolution without the need for additional satellite missions. SWOT is a collaborative satellite mission led by NASA and the French space agency CNES, with contributions from the Canadian Space Agency (CSA) and the UK Space Agency (UKSA). The mission is the first to perform a global survey of Earth's surface water and aims to provide high-resolution measurements of global surface water levels, including those of oceans, lakes, rivers and wetlands. The SWOT satellite is positioned in a non-sun-synchronous orbit at an altitude of 891 km, with a 77.6° inclination, maintaining a 21-day repeat cycle throughout its science phase (JPL, 2025c). However, during the Cal/Val phase (March 29–July 09, 2023; local date), SWOT collected data at high temporal resolution (~1-day repeat cycle). Unlike the science phase, during this period, SWOT covered only limited areas across the globe and operated at an altitude of 857 km (JPL, 2025b; JPL, 2025c). The Ka-band Radar Interferometer (KaRIn) serves as SWOT's primary instrument, operating at 35.75 GHz frequency (or 8.4 mm wavelength). KaRIn is a bistatic synthetic aperture radar (SAR) system that uses two antennas mounted at opposite ends of a 10-m boom, observing the Earth's surface at near-nadir incidence angles of approximately 1°– 4°. It operates by sending radar pulses from one antenna and receiving the return signals on both, creating interferometric pairs. This interferometric approach allows KaRIn to capture high-resolution coverage with a 120 km wide swath and a gap of about 20 km along the nadir track. Another payload, the dual-frequency (Ku & C bands) Poseidon-3C nadir radar altimeter, functions similarly to the Poseidon-3B altimeter onboard the Jason-3 mission, collecting data as a narrow 1D profile along the satellite path in the gap between the KaRIn swaths by transmitting radar pulses directly downward and analyzing the time delay and the returned signals (Fjørtoft et al., 2014; Biancamaria et al., 2016; JPL, 2025c).

Advances in microwave satellite observations (Ku- to L-band), including radar altimetry, have improved the retrievals of LIC and LIT. However, the sensitivity of Ka-band observations to snow-covered lake ice remains largely unexplored. Kouraev et al. (2015) conducted a study using SARAL/AltiKa, the first Ka-band satellite altimeter mission, and found that Ka-band signals are highly sensitive to surface conditions, effectively discriminating between open water and various lake ice types. Several sea ice studies using SARAL/AltiKa further confirmed its capability for open water and ice-type discrimination, while highlighting that its penetration is generally limited to near-surface layers (Verron et al., 2021). The SWOT mission offers a unique opportunity to further investigate the use of Ka-band altimetry for improving our understanding of lake ice and overlying snow properties. In addition, there has been a long-standing need for retrieving snow properties overlying lake ice, namely snow depth and snow mass (the product of snow depth and snow density), to improve the simulation of LIT from lake models used in standalone mode or as lake parameterization schemes in numerical weather forecasting and climate models.

https://doi.org/10.5194/egusphere-2026-4309
Preprint. Discussion started: 17 August 2026

In this study, we use Ka-band Radar Interferometer (KaRIn) data from the Surface Water and Ocean Topography (SWOT) mission, acquired over Teshekpuk Lake, Alaska, during the near-daily Cal/Val phase, to assess the sensitivity of Ka-band radar to lake ice and overlying snow properties. The paper is organized as follows. Section 2 introduces the study area and provides a detailed description of the datasets used in this study, including KaRIn, ancillary satellite, and field campaign data. Section 3 presents the analysis and interpretation of Ka-band sensitivity to lake ice and snow properties, along with a discussion of key findings. Finally, Section 4 provides conclusions and directions for future work regarding Ka-band monitoring of snow-covered lake ice.

2 Study Site and Data Description

2.1 Study Site

This study focuses on Teshekpuk Lake, the largest thermokarst lake located on the Arctic Coastal Plain of northern Alaska (Figure 1). Covering an area of approximately 850 km², the lake consists of two main basins: a deeper western basin with a maximum depth of ~7 m and a shallower eastern basin with a maximum depth of ~4 m. The lake is situated within a low-relief landscape (~1 m above sea level) characterized by continuous ice-rich permafrost and numerous thermokarst lakes and lies in close proximity to the Beaufort Sea. Despite its coastal setting, Teshekpuk Lake remains a freshwater system, primarily sustained by substantial inflow from Kealok Creek and additional drainage from the Ikpikpuk Sand Sea to the south (Arp et al., 2013; Arp et al., 2026). Teshekpuk Lake is also of high ecological importance, providing critical overwintering habitat for many fish species and supporting diverse wildlife, including caribou, geese, migratory shorebirds, bears, wolves, and foxes (Arp et al., 2010; Arp et al., 2011). Given its size, location, ecological significance, and potential as an LC-130H landing site (Jones et al., 2026), Teshekpuk Lake provides valuable context for investigating lake ice and snow dynamics in high-latitude lakes. The lake experiences a prolonged ice-covered period (>9 months), typically from early October through July (Arp et al., 2026). During the study period, the lake was observed by SWOT KaRIn along pass 026 (tile 026R), providing near-daily coverage. The study spans cycles 474–577, with data gaps during cycle 476 (March 31) and cycles 525–528 (May 19–22). These gaps were caused by a Solid State Recorder single event upset, during which no instrument data were acquired. In addition, observations from cycle 506 (April 30) were excluded due to pronounced striping artifacts that degraded data quality. To capture variability and better interpret the SWOT observations, ten sites (shown as orange circles and labelled Buffer Centre points 1–10 in Figure 1) were manually selected across Teshekpuk Lake to represent different regions, including nearshore areas and the western, central, and eastern basins. At each site, KaRIn observations within 30 m and 100 m buffers were extracted and used in both spatial and temporal analyses. A buffer is a circular area around a point location, defined by a specified radius, within which observations are extracted. The use of multiple buffer sizes was designed to capture processes at different spatial scales: the 30 m buffer to closely represent field transect locations, and the 100 m buffer to provide a representative local-scale characterization of lake conditions.

https://doi.org/10.5194/egusphere-2026-4309
Preprint. Discussion started: 17 August 2026

2.2 Data description

2.2.1 Pixel cloud data

In this study, we used Level 2 KaRIn High-Rate Pixel Cloud data (PGD0; reprocessed version D products), released on May 13, 2025. Version D (also referred to as D0) was the latest release of the Pixel Cloud (PIXC) product at the time the data were downloaded for this study (December 07, 2025). PIXC observations acquired during the SWOT Cal/Val period (March 29, 2023–July 09, 2023; local date) were used to assess the sensitivity of SWOT KaRIn measurements over lake ice and overlying snow (SWOT, 2025). During this period, acquisition times shifted by approximately 9 minutes each day. These near-daily observations are ideal for capturing lake ice processes. It is important to note that the study period covers only part of the ice phenology, from late ice growth in late March to the ice-free state in early July, thus excluding freeze-up. This PIXC product (derived from the two-dimensional KaRIn Single Look Complex images) contains the following interferogram-derived parameters for each pixel (or data point): geolocated heights, backscatter, geophysical fields, and flags. Among these, we mainly analyzed two variables: backscatter and height above the ellipsoid. The irregularly spaced PIXC data offer high spatial resolution, ranging between ~10 m (far swath) to ~70 m (near swath) in the across-track direction and ~5 to 10 m in the along-track direction. It serves as the foundational input for generating higher-level products, including Raster, Lake Single Pass (LakeSP), and River Single Pass (RiverSP) Vector shapefiles (JPL, 2025c).

https://doi.org/10.5194/egusphere-2026-4309
Preprint. Discussion started: 17 August 2026

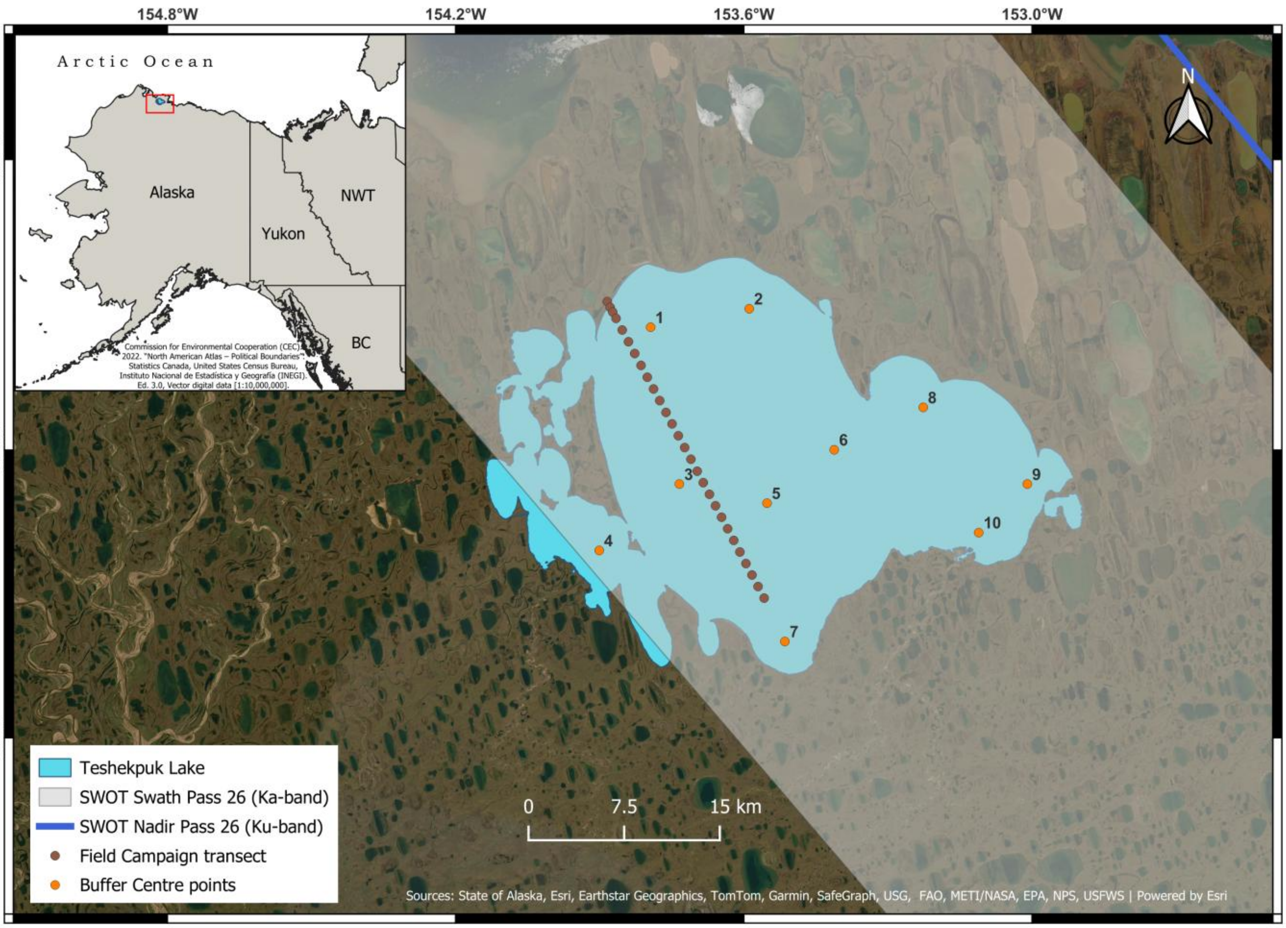

Figure 1: Study area of Teshekpuk Lake showing SWOT KaRIn coverage (grey rectangle) and nadir track (dark blue line). Orange circles indicate locations used for 30 m and 100 m buffer-based analyses, while brown circles represent in situ field observations collected along a transect on May 10, 2023.

The radar backscatter ($\mathrm{Sigma0_L}$) is derived from the interferogram and provided in the PIXC data in linear units. These linear units are converted to decibels ($\mathrm{Sigma0_{dB}}$) using Eq. (1):

$$\mathrm{Sigma0_{dB}} = 10 * \log_{10}(\mathrm{Sigma0_L}) \tag{1}$$

Surface height represents the elevation of each pixel, determined from the three-dimensional geolocation of KaRIn measurements. Heights are given in meters relative to the WGS 84 reference ellipsoid. The height values in the PIXC product include corrections for instrument calibration, signal propagation delays caused by ionospheric effects, both dry and wet tropospheric components, and adjustments from crossover calibration. In this study, water surface heights referenced to the

https://doi.org/10.5194/egusphere-2026-4309
Preprint. Discussion started: 17 August 2026

EGM2008 geoid were used. These were derived from SWOT ellipsoidal heights following the standard correction procedure described in the SWOT User Handbook (JPL, 2025c). The conversion accounts for geoid undulation and tidal effects, and the resulting geoid-referenced heights were used for all subsequent analyses. The height above geoid (H_{geoid}) is obtained by Eq. (2):

$$H_{geoid} = H_{ellipsoid} - N - (H_{solid\ earth\ tide} + H_{load\ tide} + H_{pole\ tide}) \quad (2)$$

Where $H_{ellipsoid}$ is the SWOT ellipsoidal height, N is the geoid height, and the remaining terms represent corrections for solid Earth tide, load tide, and pole tide effects, respectively.

Hereafter, backscatter refers to radar backscatter expressed in decibels (dB), and height refers to surface elevations (m) referenced to the EGM2008 geoid. In addition, we examined the classification flag variable, which is important for a more comprehensive understanding of the measurements. This variable includes the following classes: land, land near water, water near land, open water, dark water, low coherence water near land, and open low coherence water. These class types provide context for interpreting backscatter and height measurements and for understanding variability in the Ka-band response across different surface types. Although no filtering based on the classification flag was applied in this study, the classification information was considered during interpretation of the surface scattering characteristics (JPL, 2025a; JPL, 2025c).

The surface classes are determined using information derived from the KaRIn sensor together with prior information. The classification primarily relies on the automatic water detection based on the backscatter contrast between water and land surfaces. Owing to KaRIn's unique near-nadir viewing geometry and short Ka-band wavelength, water surfaces are generally more reflective than land surfaces. Since SWOT incidence angles are approximately 1°–4° off-nadir rather than exactly nadir, some degree of surface roughness is required to return sufficient energy to the radar. Wind-driven waves and ripple create a near-smooth water surface that produces quasi-specular reflection (i.e., surfaces with small-scale irregularities spreads most of the reflected energy within a narrow range of angles, allowing the off-nadir antennas to receive a strong return signal). As a result, water surfaces typically appear relatively bright. However, under low-wind conditions (wind speed less than 1 m s^{-1}), the water surface can become extremely smooth and behave more like a mirror, producing highly specular reflection. At off-nadir viewing angles, such reflections direct most of the transmitted energy away from the radar, resulting in little to no returned signal and causing the water to appear dark. This phenomenon is referred to as "dark water". Such effect may also occur when water is not detected despite being expected from prior information (external water-probability map). In contrast, land surfaces, which are generally rougher, produce diffuse scattering, where the reflected energy is distributed in multiple directions and less energy is returned toward the radar antenna (Fjørtoft et al., 2014; Biancamaria et al., 2016; Kacimi et al. 2025; JPL, 2025c).

https://doi.org/10.5194/egusphere-2026-4309
Preprint. Discussion started: 17 August 2026

2.2.2 Complementary satellite images

Complementary optical and synthetic aperture radar (SAR) image datasets were used for the interpretation of SWOT KaRIn measurements. Optical imagery included near-infrared (NIR) bands from Sentinel-2 (10 m) and Landsat 8/9 (30 m), which provide detailed information on snow and ice extent due to NIR sensitivity to surface water and snow properties (ESA, 2025; USGS 2025). For selected dates, a Landsat-9 composite using shortwave infrared (SWIR2 and SWIR1) and Red bands was generated to improve surface feature visibility. MODIS Aqua and Terra true-color imagery, with daily revisit and moderate spatial resolution, was examined to provide broad-scale temporal context for lake surface evolution and to assist in identifying seasonal transitions (NASA, 2025). However, MODIS data were not included in the results figures. To overcome the limitations of optical imagery, including sensitivity to cloud cover and dependence on sunlight, we used SAR data from Sentinel-1A and the RADARSAT Constellation Mission (RCM), whenever available, for all-weather, day-and-night monitoring (ASF, 2025; Government of Canada, 2025). Sentinel-1A Ground Range Detected High-resolution (GRDH) products provided dual-polarized (VV and VH) C-band data at approximately 10 × 10 m resolution. The RCM offered high-resolution (3–10 m), dual-polarized (HH and HV) C-band imagery.

2.2.3 Temperature data

To assess temperature conditions over the study period, we used the ERA5 Land climate reanalysis dataset produced by the European Centre for Medium-Range Weather Forecasts (ECMWF) and distributed via the Copernicus Climate Change Service (C3S). ERA5 Land provides hourly estimates of land surface and near-surface variables on a 0.1° (~9 km) grid from January 1950 to the present (Muñoz Sabater, 2019). For this study, we focused on 2 m air temperature and skin temperature to support the interpretation of the SWOT KaRIn measurements. Both variables were evaluated during exploratory analysis, with skin temperature representing surface-level conditions and 2 m air temperature capturing near-surface atmospheric conditions. As the two showed minimal differences in their temporal evolution over the period of analysis, we present results and plots primarily using 2 m air temperature. To match SWOT overpasses with ERA5 Land data, timestamps were rounded to the nearest full hour when observations fell between hourly intervals. The temperature data were then masked to the lake polygon extents to maintain spatial consistency with the SWOT measurements. This approach ensured temporally and spatially aligned temperature values, supporting accurate interpretation of the influence of surface thermal conditions on lake ice and snow as observed by SWOT.

2.2.4 Elevation data

https://doi.org/10.5194/egusphere-2026-4309
Preprint. Discussion started: 17 August 2026

To provide topographic context for the study area, ArcticDEM was used as an independent elevation dataset. ArcticDEM is a high-resolution digital surface model (DSM) of the Arctic that represents surface elevations, including vegetation, infrastructure, and other above-ground features. It is derived from stereoscopic optical imagery acquired by satellites such as WorldView-1, WorldView-2, WorldView-3, and GeoEye-1, and processed using the Surface Extraction from TIN-based Search-space Minimization (SETSM) algorithm (Porter et al., 2023). In this study, the 2 m ArcticDEM Mosaic (Version 4.1) tiles provided by the Polar Geospatial Center were used. These mosaic tiles are composited from multiple digital elevation model (DEM) strips acquired at different times. Elevations are originally referenced to the ellipsoid and were converted to EGM2008 orthometric heights (relative to the geoid) to ensure consistency with SWOT surface elevation measurements.

2.2.5 Field data

In situ measurements were used to support the interpretation of SWOT KaRIn observations. A field campaign conducted on May 10, 2023, at Teshekpuk Lake collected measurements along a ~26 km transect extending from the tundra shoreline across the lake (Jones et al., 2025). Sampling locations were spaced at approximately 1 km intervals to capture spatial variability across nearshore and central basin regions (Figure 1). All sampling points were geolocated using a differential Global Positioning System (GPS), providing high-accuracy measurements of latitude, longitude, and surface elevation (WGS84 ellipsoid height). In this study, WGS84 ellipsoid height is the primary field variable used for comparison with SWOT-derived heights. Field photographs were also collected at selected locations to document local snow and ice conditions and support qualitative interpretation of surface conditions.

3 Results and Discussion

3.1 Sensitivity of KaRIn measurements to evolving lake ice and overlying snow properties

Understanding how Ka-band Radar Interferometer (KaRIn) measurements are sensitive to lake ice and overlying snow properties is important for the development of ice/snow retrieval algorithms needed for cold region hydrology, including the evaluation and improvement of freshwater (lake and river) ice models. This section investigates the sensitivity of KaRIn backscatter and height retrievals to ice conditions (e.g., melt-freeze cycles, pressure ridges, ice break-up) and snow characteristics. It is important to note that the available SWOT Cal/Val data covers the period from late March to mid-July, which means our analysis does not encompass the freeze-up period, limiting our observations to the late ice growth to open water period. To help organize our analysis, we divided this duration into four phases based on observations from optical and radar images, and ERA5 Land data: Late Ice Growth (March 29–May 04), Early Melt (May 05–May 14), General Melt (May 15–June 06), and Break-up (June 07–July 09). These phases represent typical changes in ice and snow conditions that may affect the radar signal strength and height measurements collected by SWOT KaRIn. To better understand these interactions and to capture the full temporal variability and dynamic patterns, two animations showing the continuous progression of the

https://doi.org/10.5194/egusphere-2026-4309
Preprint. Discussion started: 17 August 2026

KaRIn measurements are included in the Video supplement (Video S1 and S2). This supplementary material provides a more detailed and comprehensive visualization of the observed changes.

3.1.1 Late ice growth

During the late ice growth phase (March 29–May 04), Teshekpuk Lake is fully ice-covered with snow, with surface conditions dominated by cold atmospheric temperatures (mean daily air temperatures range between ~ –25°C and –5°C) that promote ice thickening and the evolution of snow properties. This inference is based on the visual interpretation of complementary satellite images and ERA5 Land 2 m air temperature data. Understanding the penetration depth of Ka-band into snow is critical for interpreting the observed SWOT data. Penetration depth (δ_p) is calculated according to Eq. (3):

$$\delta_p = \frac{\lambda_0}{4\pi} * \frac{1}{\sqrt{\frac{\varepsilon'}{2}\left(\sqrt{1 + \left(\frac{\varepsilon''}{\varepsilon'}\right)^2} - 1\right)}} \tag{3}$$

where λ_0 is the wavelength, ε' is the real component of the permittivity, and ε'' is the imaginary component of the permittivity as given in Ulaby et al. (1986). Using the snow microwave radiative transfer (SMRT) model (Picard et al., 2018), the values for the real and imaginary dielectric components can be calculated for a theoretical snowpack of 0.2 m and density values ranging from 100 to 450 kg m^{-3}; these values range from 1.15+0.0001j to 1.87+0.0009j. Calculated penetration depths from these dielectric components can range from 11.75 to 1.93 m. Lake ice has a larger dielectric value, 3.17+0.003j, and a lower penetration depth of 0.74m. However, it should also be noted that past studies using ground/air-based radar systems covering Ka-band (Stroeve et al., 2020; Rodríguez-Morales et al., 2021), demonstrate that the majority of the Ka-band return is from the top of the snow indicating a limited penetration depth. Based on the theoretical and field observations, it is expected that SWOT measurements (such as height, backscatter) are a result of conditions ranging from the snow surface to limited depths within the ice cover.

An example of SWOT observations from this period is presented in Figure 2, which shows measurements acquired on April 14, 2023, over Teshekpuk Lake. Figure 2(a) illustrates the spatial variability of SWOT height and backscatter. Interestingly, throughout this phase (Video S1), both measurements are relatively higher along the western margin of the central basin (highlighted by the pink oval in Figure 2(a)) than elsewhere in the basin. This region corresponds to a shallow nearshore shelf characterized by bedfast ice conditions. Grunblatt and Atwood (2014) report that bedfast ice typically appears dark in C-band SAR imagery due to reduced dielectric contrast at the ice–frozen soil interface. Consistently, the same region exhibits distinctly low backscatter in Sentinel-1 C-band SAR imagery (Figure 2(b)), further supporting the interpretation of bedfast ice. The higher elevations and backscatter observed in SWOT (pink oval) are therefore associated with shallow bathymetric conditions where ice freezes to the lake bottom. The contrast in backscatter between bedfast and floating ice also suggests that the SWOT

https://doi.org/10.5194/egusphere-2026-4309
Preprint. Discussion started: 17 August 2026

KaRIn signal may not be strictly limited to the ice surface and could exhibit some degree of penetration into the ice cover. Overall, these results highlight SWOT's ability to clearly distinguish between bedfast and floating ice conditions based on backscatter and elevation characteristics. In addition, a consistent height contrast is observed between the Teshekpuk Lake and the surrounding terrain during this phase (and across all other phases), with the lake surface remaining lower than the adjacent land. This pattern likely reflects the lake occupying a local topographic depression, while the surrounding bluffs and terrain are relatively higher and more heterogeneous, as also indicated by the DEM shown in Figure 2(c). Environmental processes such as wind redistribution of snow from the smoother lake surface to the rougher tundra, along with possible snow trapping by vegetation or dunes, may also contribute to the observed higher surface heights over land. Due to lower heights relative to the land, the surrounding thermokarst lakes are also clearly identifiable, as seen in Figure 2(a). The clear contrast between the lake and the surrounding terrain underscores SWOT backscatter's ability to capture lake extents and characterize spatial heterogeneity in surface conditions. In Figure 2(a), backscatter shows a cross-swath gradient, with higher values in the near range (east) and lower values in the far range (west). This pattern is likely related to variations in incidence angle across the SWOT KaRIn swath, where lower incidence angles in the near range may enhance backscatter, whereas higher angles in the far range may reduce it (Fjørtoft et al., 2014; Armitage & Kwok, 2021). However, surface roughness and ice/snow variability may also contribute to this pattern.

https://doi.org/10.5194/egusphere-2026-4309
Preprint. Discussion started: 17 August 2026

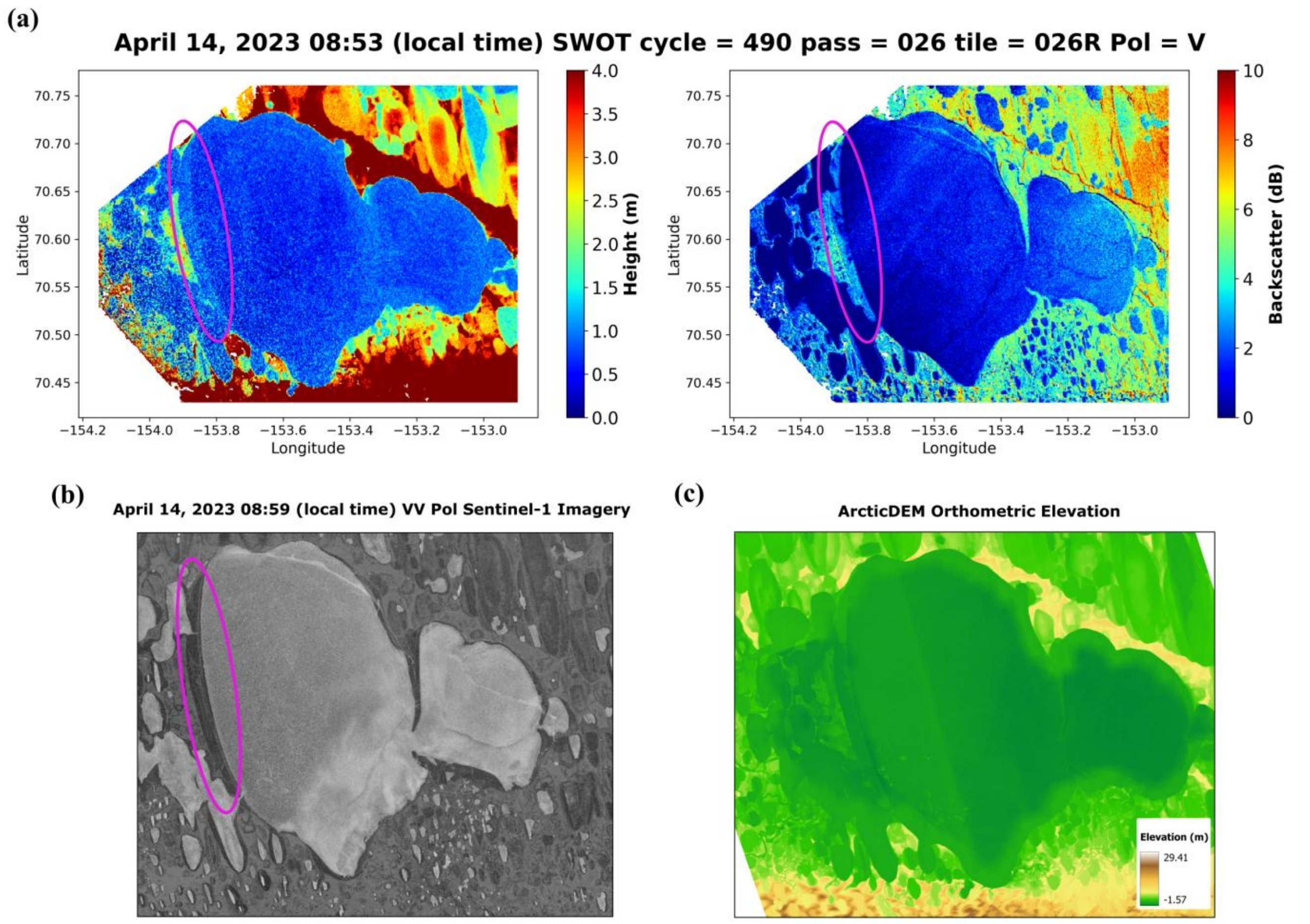

Figure 2: SWOT KaRIn observations over Teshekpuk Lake on April 14, 2023, during the late ice growth phase. (a) Surface height (m relative to the EGM2008 Geoid) and SWOT backscatter (dB). (b) Corresponding Sentinel-1 VV Pol image acquired on the same day at a similar time. The pink oval indicates the presence of bedfast ice along the margin of the central basin. (c) Orthometric elevation from ArcticDEM showing the topographic depression occupied by the lake and the surrounding higher terrain, consistent with SWOT height measurements (a).

To quantify the response of SWOT signals and assess their spatial variability across the lake, boxplots (Figure 3) are used to examine the variability of surface elevations and backscatter values within 100 m buffers at 10 sites (locations shown in Figure 1). The boxplots of SWOT heights (Figure 3(a)) show that buffer 4 exhibits the highest variability among all sites, with a wide range extending to values as low as approximately −2 m, indicating substantial heterogeneity in the retrieved elevations. Buffer 7 also shows increased variability relative to the other buffers, although with a less pronounced range. This enhanced variability in both buffers suggests more complex surface conditions, potentially associated with spatial variability in snow properties. These two buffers also show median elevations exceeding 1 m relative to the geoid, whereas most other buffers have median

https://doi.org/10.5194/egusphere-2026-4309
Preprint. Discussion started: 17 August 2026

values less than or equal to 1 m. Despite similar median values across many sites, the differences in range and interquartile spread indicate spatial variability in surface conditions, likely indicating variations in snow properties (e.g., density and structure), which can influence the effective scattering surface (i.e. within or at the top of the snowpack) and consequently, the retrieved height. Unlike the SWOT height measurements, which exhibit strong local variability at short spatial scales (notably in buffers 4 and 7), backscatter variability is more gradual and basin-scale in nature. Median backscatter values are generally clustered between 0 and 3 dB, indicating broadly consistent scattering conditions at the lake scale. However, buffers 2, 8, and 9 show slightly elevated median backscatter relative to the other sites, suggesting a coherent spatial pattern of enhanced backscatter in the eastern basin and nearshore areas.

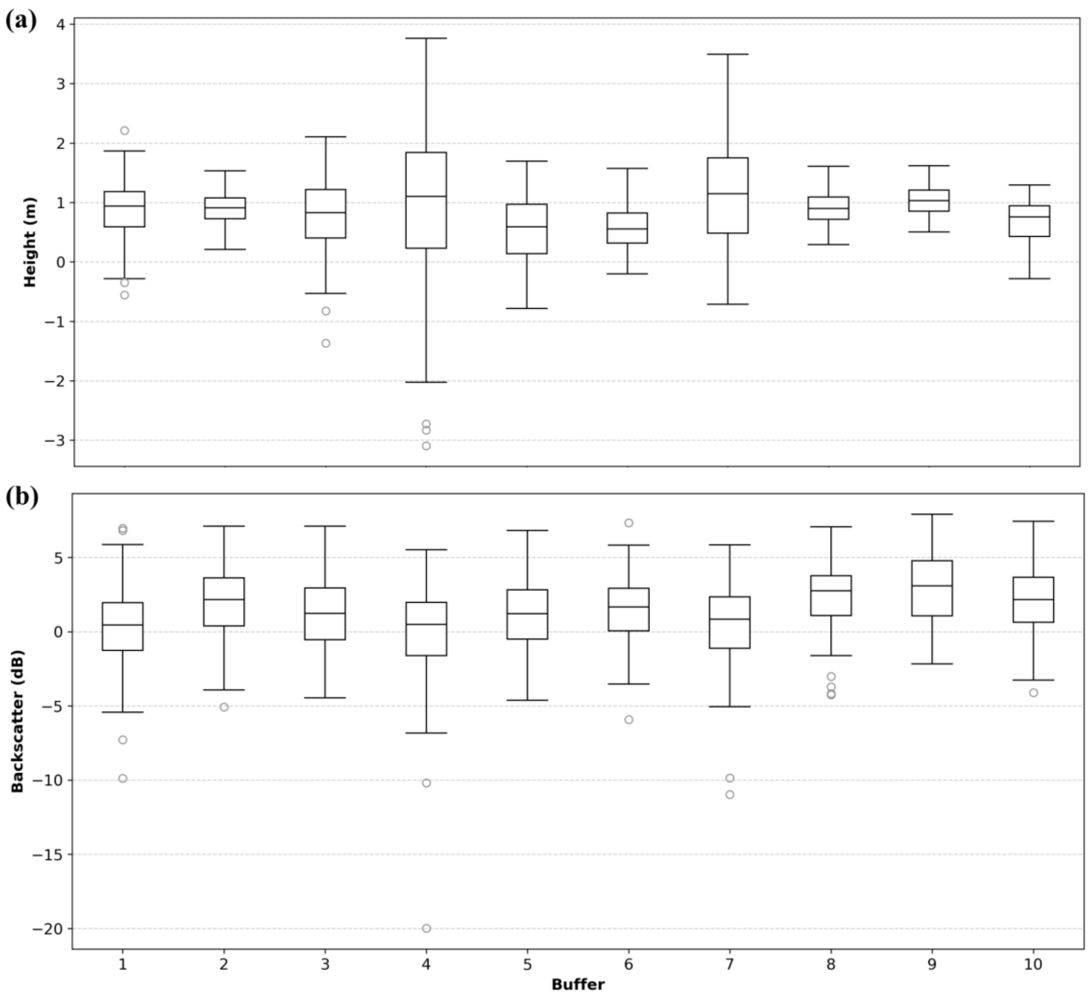

Figure 3: Distribution of SWOT height and backscatter (PIXC) values within 100 m buffers 1–10 on April 14, 2023, presented as boxplots; corresponding buffer locations are shown in Figure 1.

https://doi.org/10.5194/egusphere-2026-4309
Preprint. Discussion started: 17 August 2026

3.1.2 Early melt

As temperatures begin to rise in early May (from approximately −5 °C to above 0 °C), Teshekpuk Lake enters the early melt phase (May 05–May 14). This period is characterized by increasing solar radiation and progressive changes in snow and ice properties, marking the transition from ice growth to the onset of surface melt. Although the lake remains ice-covered, ERA5 Land 2 m air temperatures steadily increased toward 0 °C, accompanied by gradual increase in backscatter over Teshekpuk Lake and the surrounding region (Video S1). This pattern may indicate progressive surface warming and evolving snow and ice conditions associated with the onset of melt. As shown in Figures 4(a) and 5(a), SWOT-derived elevations exhibit increased spatial variability across the lake, generally ranging from approximately 0–2 m, with a notable exception in the western basin. This portion, connected to the central basin, exhibits greater variability and a broader elevation range (approximately –1.5 to 4 m), suggesting more heterogeneous surface conditions. The presence of a grounded (bedfast ice) ice shelf between these two basins may also contribute to the observed variability. In contrast, backscatter (Figures 4(a) and 5(b)) reveals pronounced spatial variability, possibly reflecting differences in surface roughness and wetness, with most of the lake showing values between –3 and 8 dB. Two prominent low-backscatter patches (Figure 4(a)) are observed in the northern part of the central basin. These patches remained spatially consistent and maintained a similar extent throughout the early melt phase (Video S1), suggesting that they are likely associated with persistent surface-related conditions, such as spatial variations in snow or ice properties. The same features are also clearly visible in the Landsat composite of shortwave infrared (SWIR-2, SWIR-1) and red bands (Figure 4(c)). These regions may contain relatively lower snow depth and denser snow cover (larger grains), which could enhance volume scattering and contribute to the observed lower backscatter values (Hall et al., 2005; Krol & Löwe, 2016). Alternatively, the two low-backscatter patches may be associated with localized accumulation of meltwater on the lake ice (shallow surface ponding) or the development of wet or slushy conditions beneath the snow. In addition, similar to the late ice growth phase (Figure 2(a)), backscatter is highest near-nadir and decreases with increasing incidence angle. However, during the present phase (Figure 4(a)), this angular dependence is more pronounced, possibly reflecting evolving surface melt conditions compared to the relatively stable ice conditions observed previously.

https://doi.org/10.5194/egusphere-2026-4309
Preprint. Discussion started: 17 August 2026

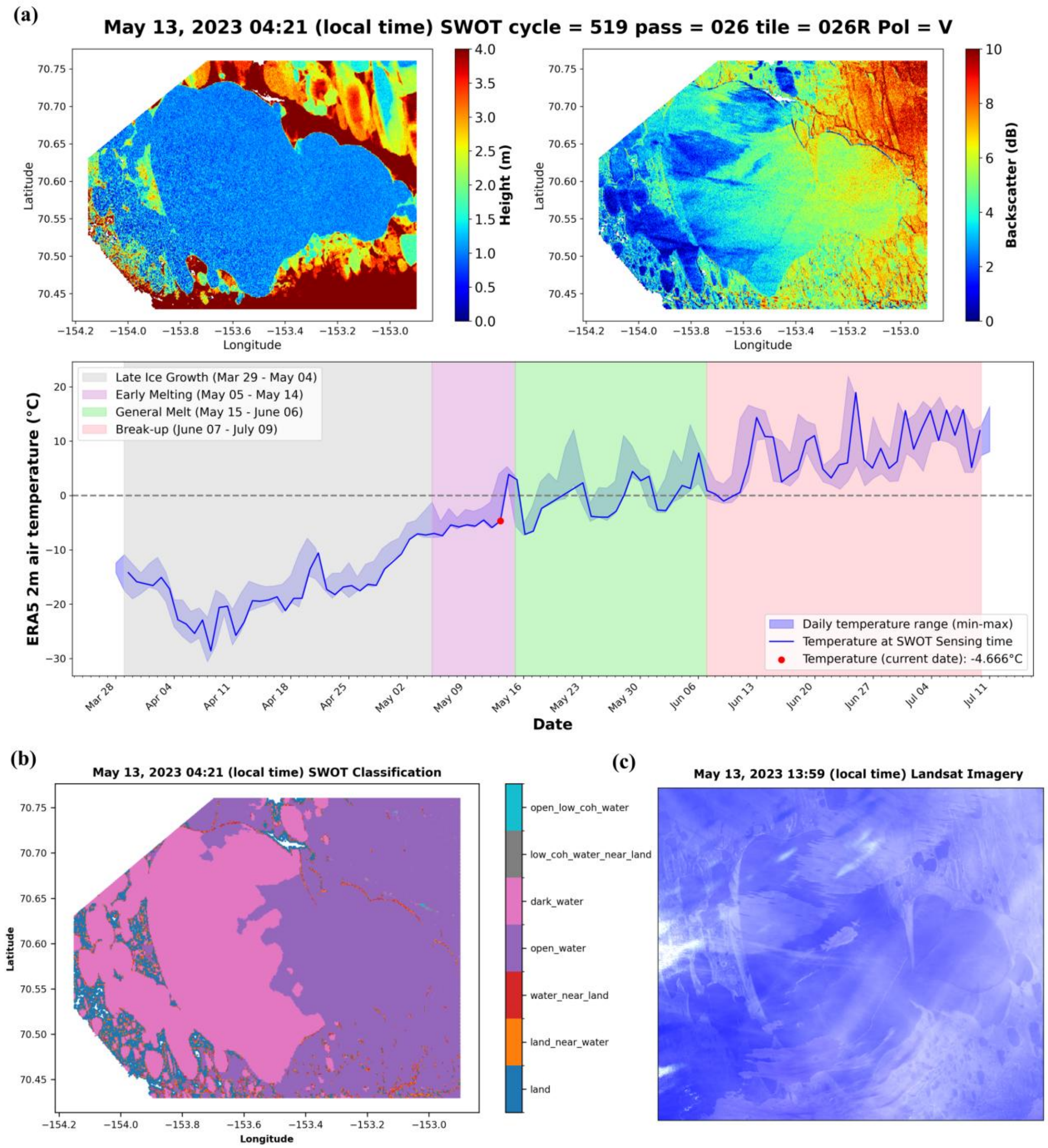

Figure 4: An example of SWOT KaRIn observations over Teshekpuk Lake during the early melt phase on May 13, 2023. (a) Surface height (m), backscatter (dB), and ERA5 2 m air temperature (°C) time series with the SWOT acquisition time highlighted. (b) SWOT classification flags. (c) Landsat-9 composite (SWIR-2, SWIR-1, and Red bands) showing two low-backscatter patches identified in the SWOT backscatter.

https://doi.org/10.5194/egusphere-2026-4309
Preprint. Discussion started: 17 August 2026

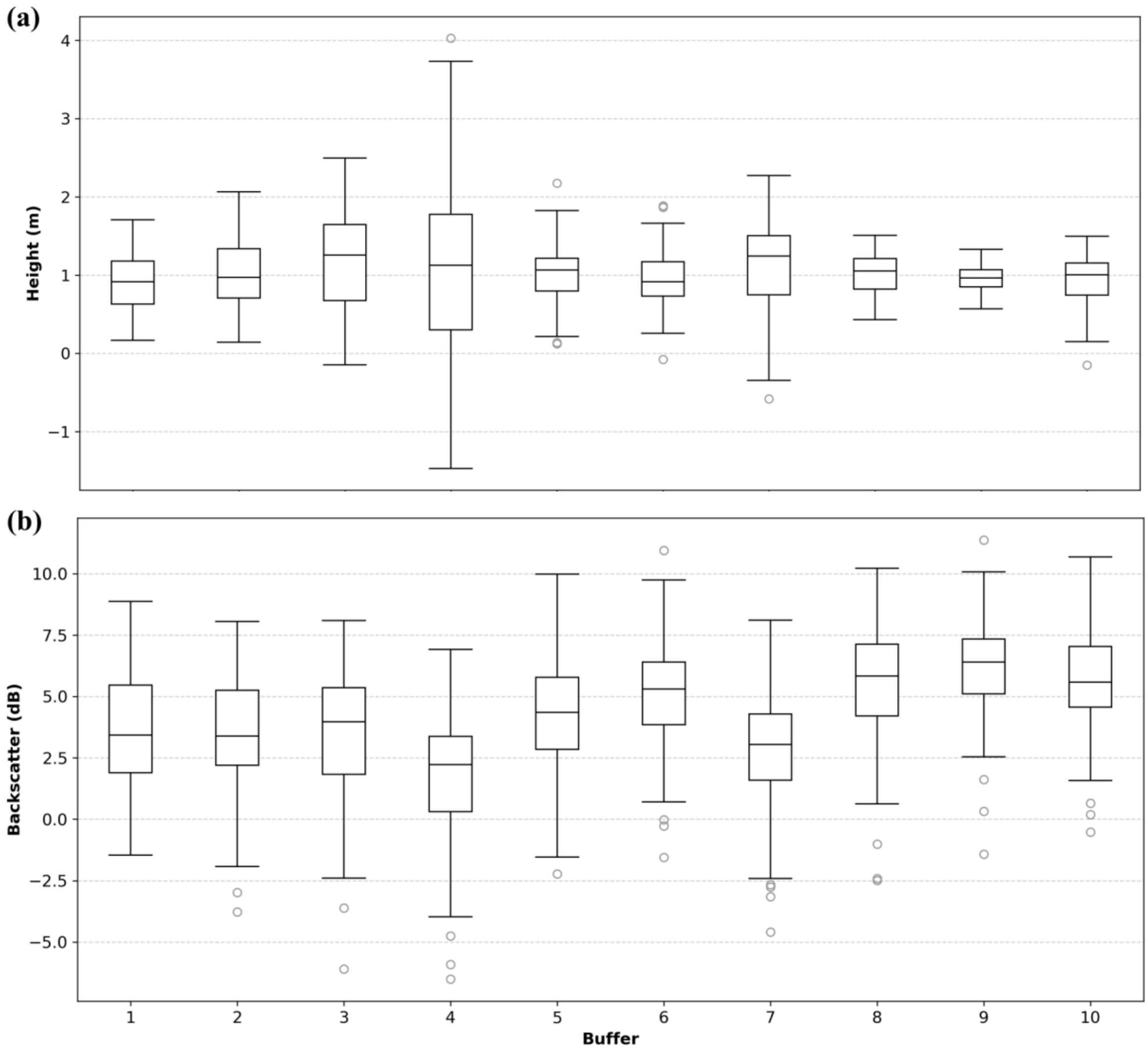

355 **Figure 5: Distribution of SWOT height and backscatter (PIXC) values within 100 m buffers 1–10 on May 13, 2023, presented as boxplots; corresponding buffer locations are shown in Figure 1.**

In contrast, these spatial variations in backscatter are not reflected in the KaRIn height measurements. The height remains similar to the previous phase, with only minor variations across the lake. This suggests potential limitations in height retrieval under wet or evolving surface conditions. The classification flags (Figure 4(b)) provided in the PIXC data was designed to aid interpretation of the surface types. However, in our study area, particularly fully ice-covered period, these flags provide limited additional information on the surface condition. Most of the regions is classified as either open water or dark water (Video

https://doi.org/10.5194/egusphere-2026-4309
Preprint. Discussion started: 17 August 2026

S2). Some small thermokarst lakes and part of the lakes can be identified from the classification map, although not properly labelled. This suggests that the current classification scheme may not adequately capture the diversity of snow and ice surface types present, highlighting the need for improved or additional classes to better represent these conditions. While the "water near land" and "land near water" classes somewhat delineate water bodies, the "land" class appears to represent only a limited portion of the surrounding terrestrial areas. A previous analysis of version C0 of SWOT KaRIn data by the authors (not shown) over the same region and period, revealed that the regions classified as dark water (i.e., smooth, mirror-like surfaces that return no radar signal) exhibited height values significantly different from those of open water class areas. These differences appeared as discontinuities in height within Teshekpuk Lake. The artifact was traced to a bug in the PIXC processing chain that led to incorrect height estimation for pixels that were not phase unwrapped. This issue has been resolved in version D, which is used in this study, where such artificial height contrasts between open water (bright) and dark water are longer observed (JPL, 2025b).

3.1.3 General melt

By mid-May, Teshekpuk Lake enters the general melt phase (May 15–June 06). This period is marked by more pronounced signs of melt. Daytime temperatures often exceed 0 °C, accelerating the melting of snow and lake ice surface, while nighttime cooling allows for intermittent refreezing. These diurnal freeze-thaw cycles, as captured by SWOT KaRIn backscatter measurements and ERA5 reanalysis, are likely to result in changes to snow conditions, e.g., higher moisture content, changes in grain size, density, and ice crusts (Benson and Sturm, 1993), which, based on the expected behaviour of Ka-band, should impact SWOT KaRIn backscatter and height. Similarly, Howell et al. (2009) observed distinct backscatter oscillations in Ku-band QuikSCAT data over Great Bear and Great Slave Lakes, attributing them to temperature-driven freeze–thaw cycles on lake ice, where warming increased liquid water content (lowering backscatter) and subsequent cooling enabled refreezing (increasing backscatter). KaRIn observations were acquired between approximately 00:30 and 04:00 local time. The timing of these acquisitions is important for interpreting the surface conditions at the time of observation – here, likely overnight refreezing. Figure 6 shows that the height measurements still indicate a median height of ~1 m across the lake and provide no additional insights beyond those observed in the earlier phases. In contrast, the KaRIn backscatter exhibits a strong sensitivity to surface transitions. During melt periods, backscatter values over the lake drop significantly (median ranges between –7 and 0 dB), resulting in low-return, dark surfaces (Figure 6a). Similar behaviour is also observed across the surrounding terrain, possibly indicating increased moisture content or wet snow conditions in surface layers. In subsequent refreezing episodes, backscatter values increase to be centered around –2 to 1 dB, enhancing the visibility of surface features such as ridges and rough ice (Figure 6b). Notably, the surrounding land often exhibits comparatively higher backscatter than the lake surface during these times (Video S1), consistent with the previously discussed incidence-angle dependence. This contrast likely reflects spatial variability in snowmelt and surface wetness across the tundra, where higher-elevation areas tend to dry more

https://doi.org/10.5194/egusphere-2026-4309
Preprint. Discussion started: 17 August 2026

rapidly than low-lying zones and adjacent lakes. In particular, exposed or partially exposed high-centered ice-wedge polygon terrain around the lake may contribute to enhanced backscatter over land relative to the lake surface.

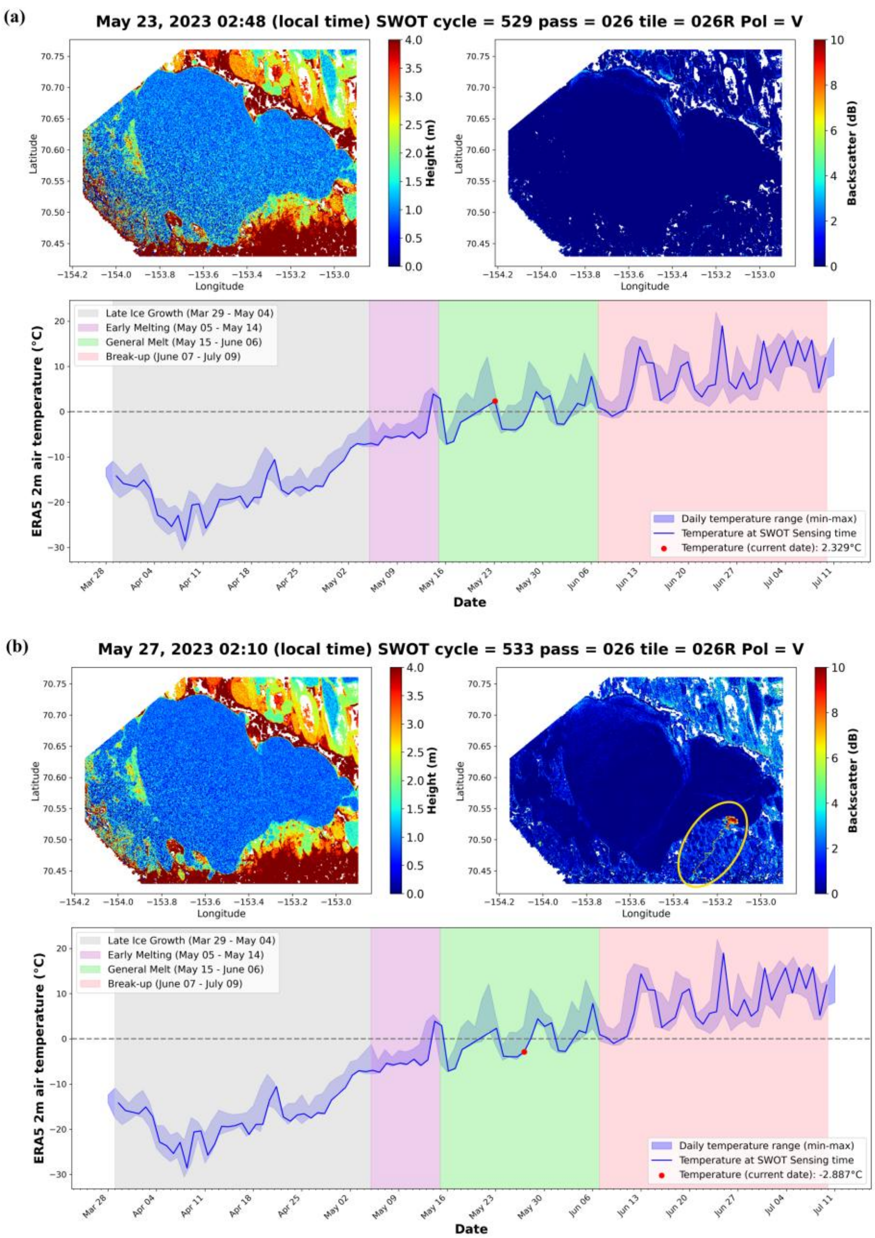

Figure 6: SWOT KaRIn observations over Teshekpuk Lake showing short-term melt and refreezing episodes during the general melt phase: (a) melt event on May 23, 2023, and (b) refreezing event on May 27, 2023. The yellow oval in (b) indicates the inlet from Kealok Creek entering the frozen lake.

https://doi.org/10.5194/egusphere-2026-4309
Preprint. Discussion started: 17 August 2026

A hydrologically significant feature emerges during this phase: a stream inlet (Kealok Creek) becomes visible near the shallow delta at the southern end of the eastern basin. The feature is first observed as an elongated zone of enhanced backscatter extending toward the lake, followed by the development of a localized bright spot (>8 dB) within the lake near the inlet. Over time, this feature expands and spreads radially into the lake (represented as a yellow oval in Figure 6(b) and 7(a)). Meltwater from the Kealok drainage likely flows onto the lake ice through the shallow delta, promoting surface melt and initiating a top-down melting process near the inlet. As melting progresses, the ice becomes increasingly buoyant, may locally detach, and subsequently transitions into floating ice that melts rapidly. Figure 7(a) also suggests that the inlet may be partially frozen, which likely results in increased slush and water input into the lake, that changes surface conditions and influences radar backscatter in the affected area.

https://doi.org/10.5194/egusphere-2026-4309
Preprint. Discussion started: 17 August 2026

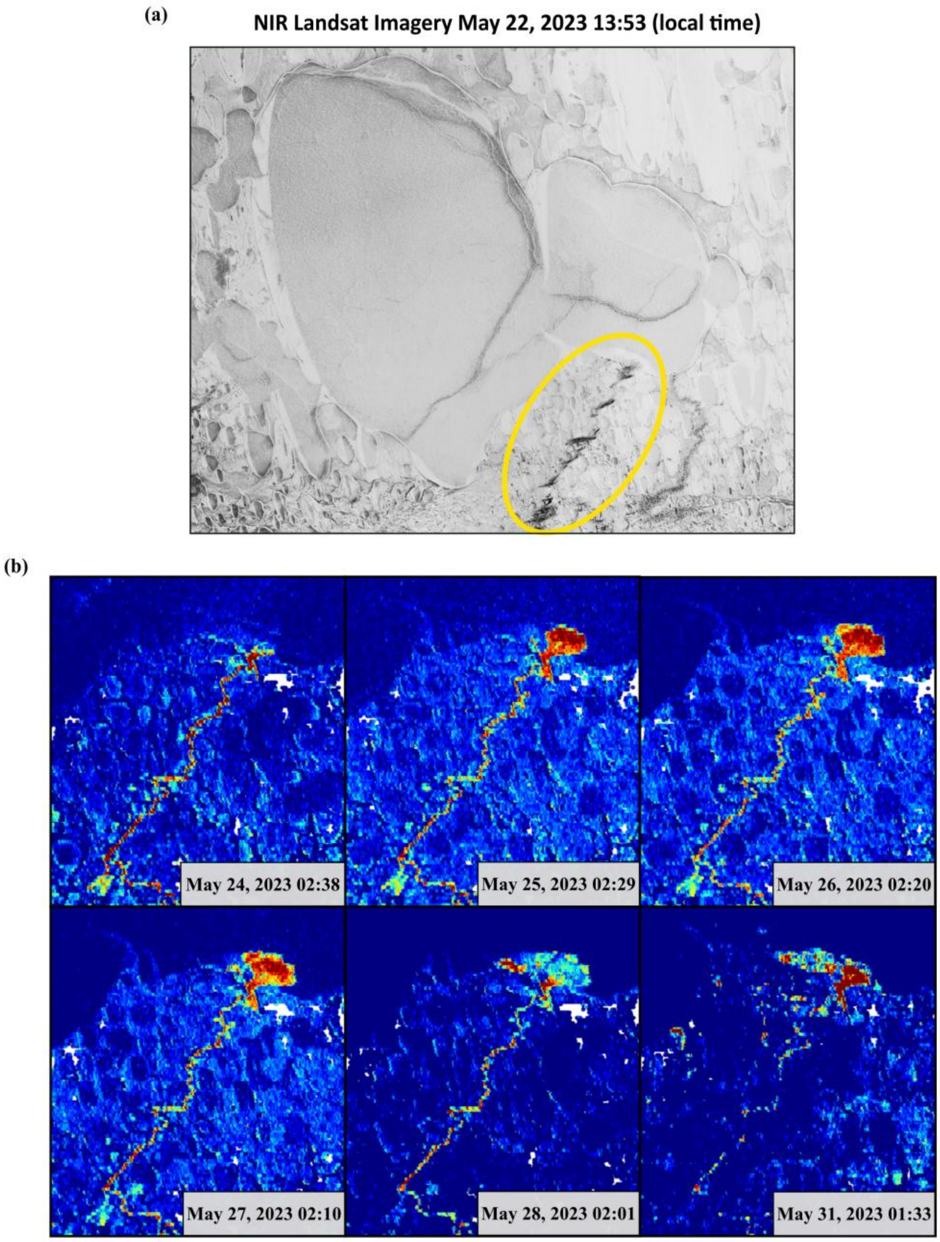

Figure 7: Spatial and temporal evolution of inflow from Kealok Creek into Teshekpuk Lake during the general melt period. (a) Landsat NIR imagery acquired on May 22, 2023, showing the creek inflow entering the lake (yellow oval). (b) SWOT KaRIn backscatter (dB) from May 24–31, 2023, showing the progressive lateral expansion of the inflow within the lake.

https://doi.org/10.5194/egusphere-2026-4309
Preprint. Discussion started: 17 August 2026

3.1.4 Break-up

During the break-up phase (June 07–July 09), air temperatures consistently exceed 0°C, leading to rapid ice decay and a widespread transition to open water conditions. Figure 8 clearly shows substantial transformations in both the SWOT KaRIn backscatter and height products during this period. At the onset of break-up, open water is already evident near the lake margins, where shallower, bedfast ice regions tend to melt earlier, as well as in the area where the Kealok Creek flows into Teshekpuk Lake (see Figure 8 and Video S1). These open water areas exhibit elevated backscatter values (shown in red), consistent with the expected response of open water under SWOT KaRIn's near-nadir and Ka-band wavelength configuration (Fjørtoft et al., 2014; Biancamaria et al., 2016; JPL, 2025c). In contrast, regions dominated by melting or floating ice exhibit much lower backscatter values (likely diffuse scattering), appearing dark blue and allowing clear delineation between open water and ice. Both open water (shown in blue) and melting ice (shown in mixed colours) extent are also identifiable in the SWOT height measurements. Melting ice generally exhibits higher heights than open water, consistent with the buoyant nature of floating ice. However, in some regions, ice surfaces are 1–2 m higher than adjacent open water, which is highly unrealistic. This discrepancy may be associated with evolving surface conditions during the melt period, as well as uncertainties in SWOT KaRIn height retrievals over heterogeneous or partially melting surfaces. Cracks (narrow open water areas formed by the divergence or convergence of ice floes caused by the degradation of lake ice pressure ridges) are evident in both SWOT backscatter and height. In addition, visible differences in backscatter values within the small thermokarst lakes near Teshekpuk Lake suggest that some areas have become ice-free. These interpretations are supported by optical imagery in Figures 8(b) and 8(c).

https://doi.org/10.5194/egusphere-2026-4309
Preprint. Discussion started: 17 August 2026

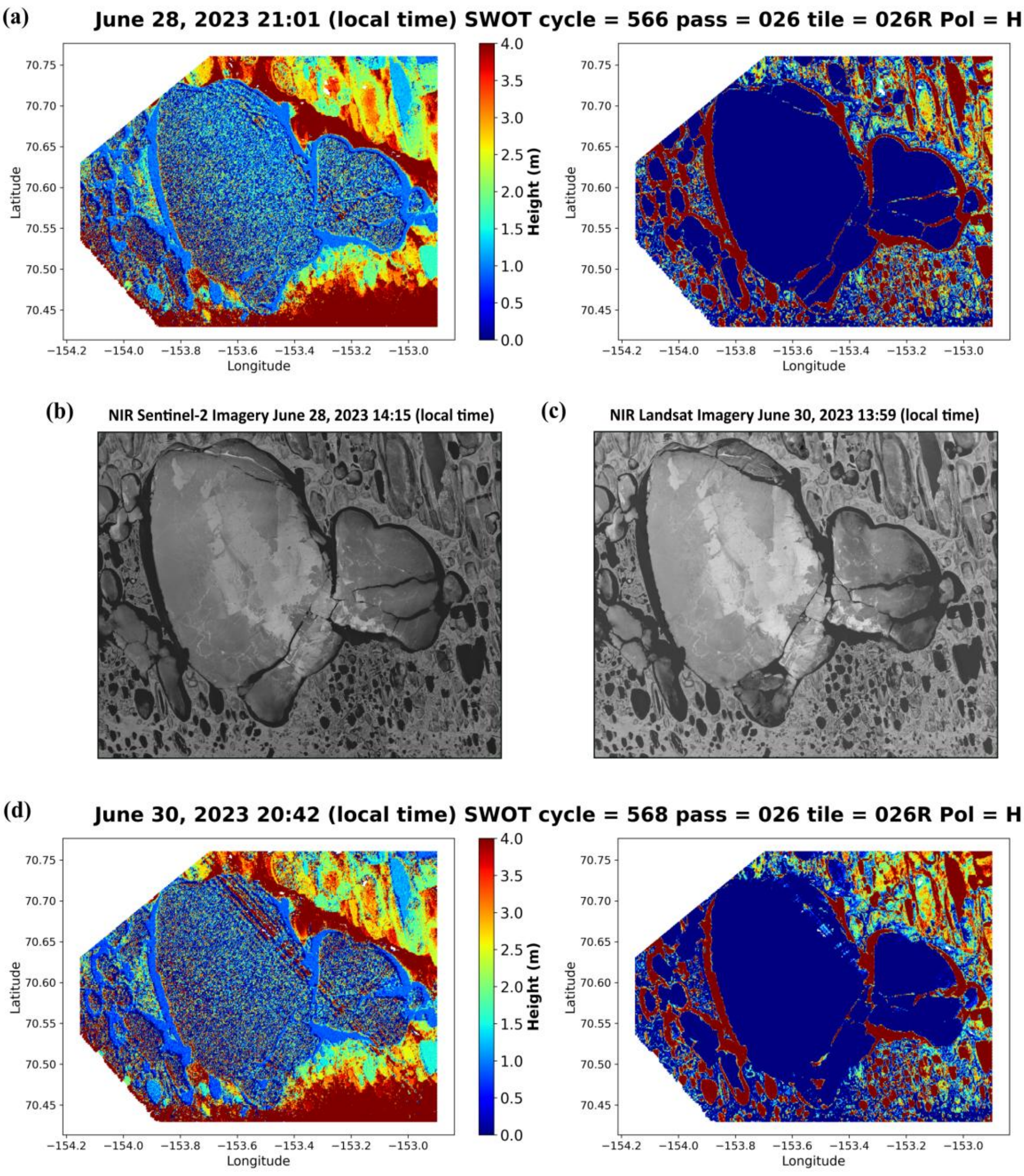

440 **Figure 8: SWOT KaRIn observations over Teshekpuk Lake during the break-up period. (a) Surface height and backscatter from SWOT (June 28, 2023). (b) Sentinel-2 image (June 28, 2023). (c) Landsat image (June 30, 2023). (d) SWOT height and backscatter (June 30, 2023) showing specular ringing artifacts in both variables.**

https://doi.org/10.5194/egusphere-2026-4309
Preprint. Discussion started: 17 August 2026

Specular ringing, visible as rough-textured linear features across the lake in Figures 8(a) and 8(d), is observed in SWOT measurements once open water starts to appear within the sensing area. This artifact arises when strong specular echoes from bright near-nadir targets contaminate adjacent measurements within the swath, leading to errors in both SWOT height and backscatter. The intensity of ringing varies with the strength of the near-nadir bright returns (JPL, 2025c). For instance, in Figure 8(a), scattering is likely less specular, and the ringing effect is weak in height and barely visible in backscatter. In contrast, in Figure 8(d), the ringing is clearly pronounced in both height and backscatter, indicating stronger near-nadir reflections, likely due to increased open water extent on June 30 compared to June 28. Figures 8(b) and 8(c) show corresponding optical observations of Teshekpuk Lake during the break-up phase, with partially open water and floating ice conditions.

3.2 Special Cases

3.2.1 Pressure ridges

Surface features such as pressure ridges are compression ruptures that form due to large temperature variations, i.e., lateral expansion during freezing and contraction during warming/melting periods. Such ice deformation features commonly develop in large lakes during freeze-up in high-latitude cold environments (Rangel et al., 2025; Arp et al., 2026; Jones et al., 2026). In the SWOT KaRIn backscatter image (Figure 9a), five distinct pressure ridges were identified by their linear structure and their contrasting radar returns relative to the surrounding ice surface. Four of these ridges (the lower ridge within the pink rectangle, two within the brown rectangle, and one within the yellow rectangle) appear as narrow, elongated zones of reduced backscatter intensity. Initial observations over sea ice environments support the lower backscatter from similar ridge features and lower backscatter from cracks/leads (Fischer et al., 2025; Kacimi et al., 2025), and this is further reinforced by SWOT documentation that states rougher surfaces will result in lower backscatter (JPL, 2025c). One exception is the fifth pressure ridge located at the north end of the lake (Figure 9b, pink rectangle) that exhibits higher backscatter compared to the surroundings. This suggests that the scattering surface at this location is smoother, however, this is difficult to confirm without in situ observations. Possible explanations could relate to the snow conditions at this location which may impact the penetration depth (see Section 3.1). The presence of these features is also visible in the Sentinel-1 SAR image acquired on the same date (Figure 9b). In SAR imagery, these deformation features result in high backscatter due to increase in scattering compared to the smoother surroundings. However, as seen in Figure 9c, complex deformation environments may impact the return to the sensor and result in darker linear features. Furthermore, field observations (Figure 9c) conducted during the field campaign on May 10, 2023, confirmed the presence of a pressure ridge at one of these locations (indicated by yellow rectangle). Indeed, a picture taken during the site visit shows the raised, fractured ice typical of pressure-ridge formation, thereby providing in situ evidence consistent with the satellite observations.

https://doi.org/10.5194/egusphere-2026-4309
Preprint. Discussion started: 17 August 2026

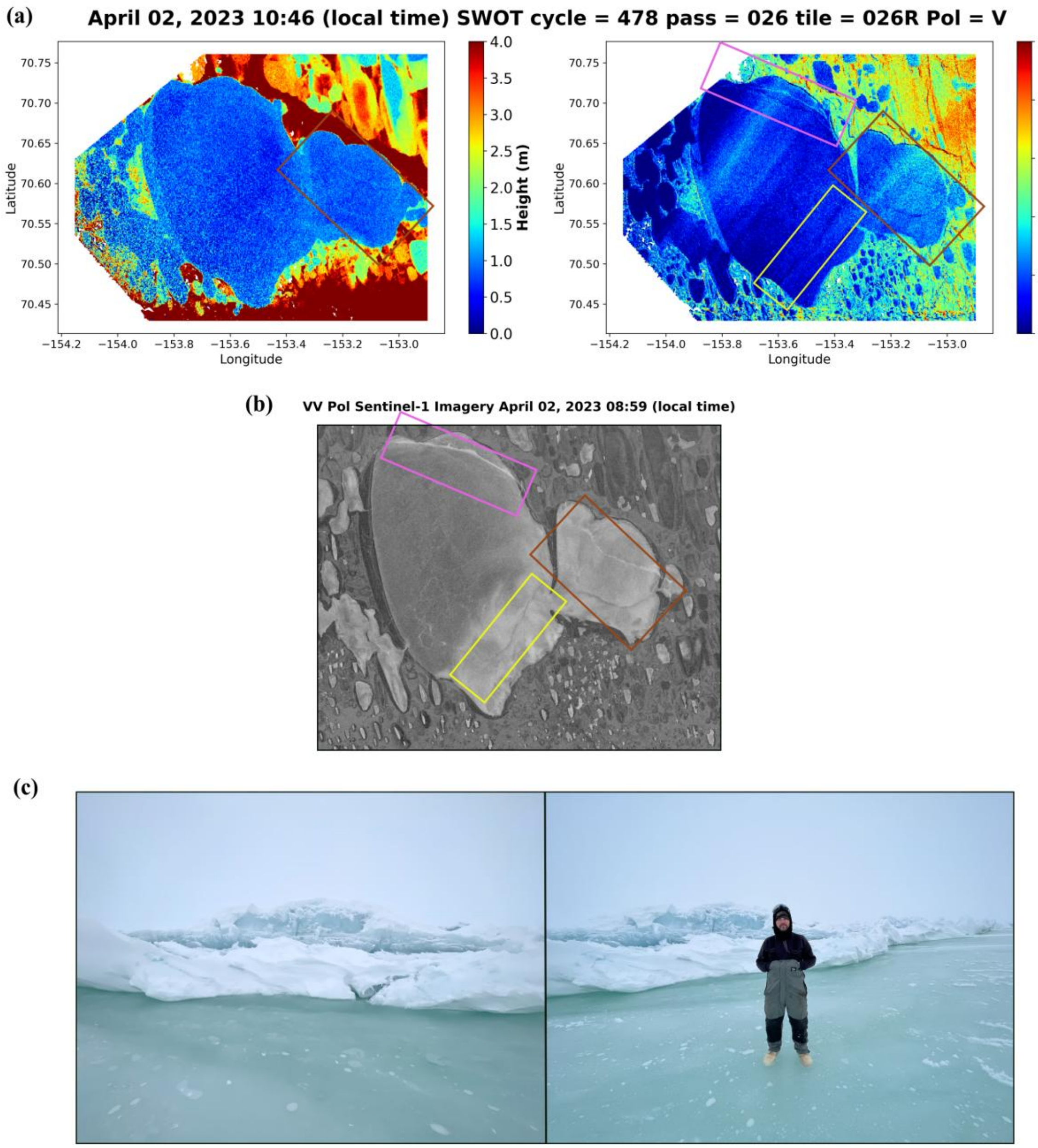

Figure 9: Pressure ridges on Teshekpuk Lake observed from: (a) SWOT KaRIn height and backscatter on April 02, 2023, (b) Sentinel-1 SAR imagery on April 02, 2023, and (c) field photograph taken on May 10, 2023, showing the pressure ridge within the yellow rectangle. The deformation features are outlined by colored rectangles.

https://doi.org/10.5194/egusphere-2026-4309
Preprint. Discussion started: 17 August 2026

3.2.2 Wind effect

Wind plays a significant role in influencing SWOT KaRIn backscatter due to the short Ka-band (8.4 mm) wavelength (Fjørtoft et al., 2014). As the lake becomes increasingly ice free, the exposed water surface becomes more sensitive to wind forcing, which strongly influences surface roughness and radar return. Previous studies over inland lakes using AirSWOT and SWOT KaRIn observations (e.g., Fayne & Smith, 2023; Trudel et al., 2024) have shown that low wind speeds (less than 3 m s^{-1}) can produce very low backscatter values. Fayne & Smith (2023) further noted that wind speeds of approximately 3 m s^{-1} or greater are generally required to generate sufficient water-surface roughness for stronger backscatter and coherence, thereby improving water-surface elevation retrievals. In Figures 10(a) and 10(c), SWOT KaRIn height measurements show anomalously high values (denoted in dark red) over portions of the lake. However, the corresponding RADARSAT Constellation Mission imagery in Figure 10(b) indicates that these regions are largely ice free, suggesting that the observed elevations are unrealistically high for open water surfaces.

Consistent with these findings, spatial comparison of the height anomalies observed on July 05 and July 09 (Figure 10) with corresponding backscatter values indicates that these are notably low (backscatter ranging from ~0 to −20 dB). These conditions are indicative of very calm or low-wind environments, where smooth water surfaces promote mirror-like specular reflection (dark water), thereby causing no radar return and degrading height-retrieval performance. The anomalous elevations observed are therefore likely artifacts associated with low wind conditions rather than true variations in water level (JPL, 2025c). These results highlight the importance of accounting for surface conditions when interpreting SWOT data. Misinterpreting wind-induced artifacts as genuine water level changes may lead to significant errors in analysis. Integrating SWOT observations with co-temporal SAR imagery and ancillary environmental data (e.g., wind speed and direction) can improve the reliability of interpretation, particularly during transitional periods when surface conditions are rapidly evolving.

https://doi.org/10.5194/egusphere-2026-4309
Preprint. Discussion started: 17 August 2026

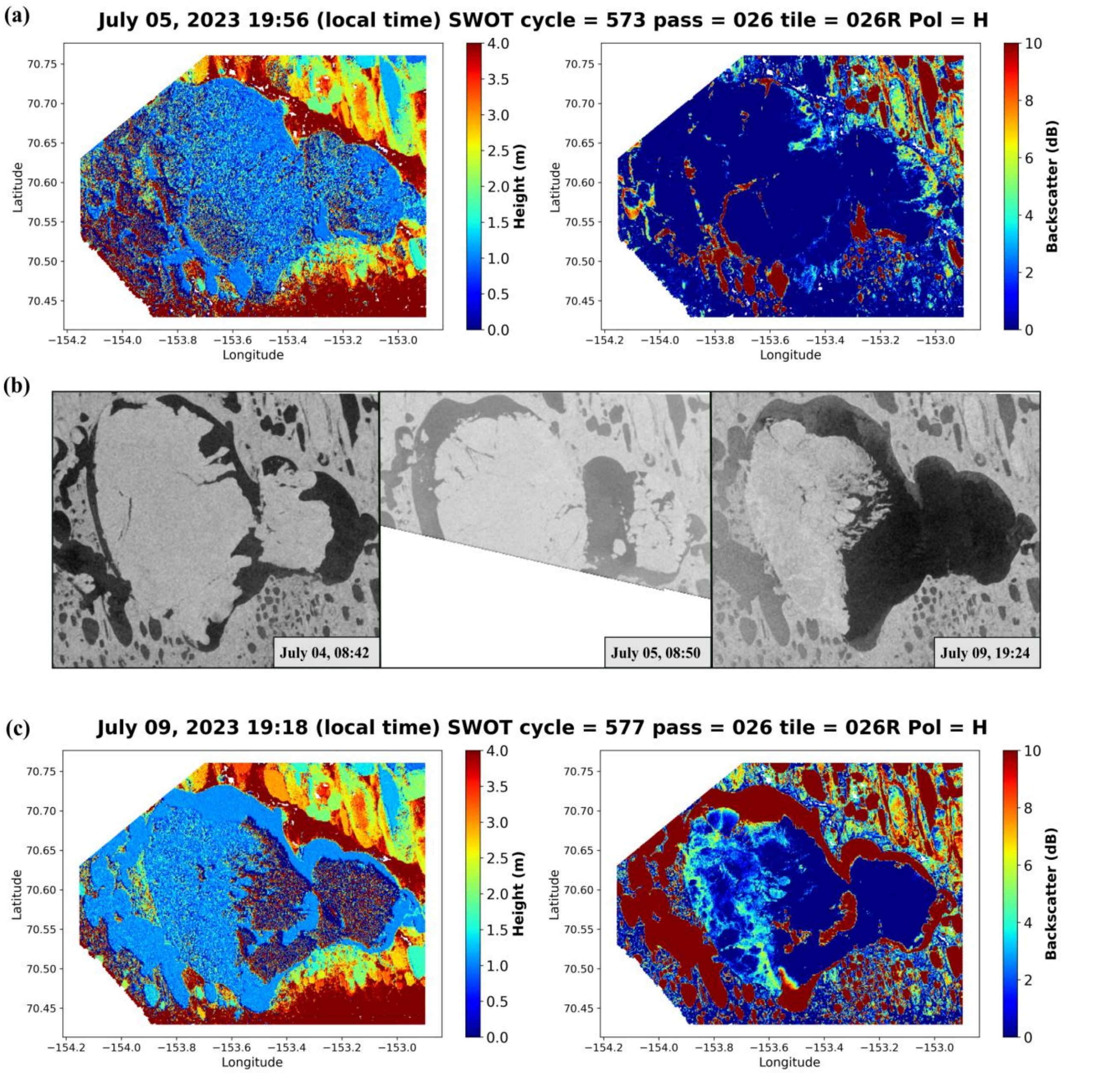

505 **Figure 10: Wind effects on Teshekpuk Lake during the break-up phase with open water and floating ice. (a) SWOT surface height and backscatter on July 05, 2023. (b) RCM imagery acquired on July 04, July 05, and July 09, 2023. (c) SWOT surface height and backscatter on July 09, 2023.**

https://doi.org/10.5194/egusphere-2026-4309
Preprint. Discussion started: 17 August 2026

3.3 Backscatter and Height Timeseries Analysis

Sections 3.1 and 3.2 highlighted possible linkages between SWOT KaRIn backscatter, height, and different phases of ice phenology. To further investigate the temporal evolution of these variables, 10 sites (shown as orange circles and labelled Buffer Centre points 1–10 in Figure 1) were selected across the lake. At each site, all KaRIn data points within a 100 m buffer were extracted, and SWOT measurements values were averaged to reduce local variability and noise. The selected sites are spatially distributed to provide representative coverage of different regions of the lake.

As shown in Figure 11, during the late ice growth period, backscatter across all sites predominantly decreases with minor fluctuations, before gradually increasing toward the end of the phase. The backscatter values decrease from approximately 1–4 dB to –2.5–1 dB during the first three-quarters of the period, followed by a gradual increase to around 0–4 dB towards the end of the phase. This behaviour likely reflects evolving snowpack properties overlying the ice, including changes in snow grain size, density, and internal layering. At Ka-band frequencies, scattering is strongly sensitive to surface and near-surface layers, along with volumetric heterogeneity within the snowpack. During the late ice growth phase in late March, the snowpack overlying the ice is expected to consist of aged winter snow that has undergone prolonged metamorphism. Such snow is typically characterized by larger grain sizes, increased density, and well-developed internal layering. These properties may enhance volume scattering within the snowpack, resulting in lower backscatter (Hall et al., 2005; Krol & Löwe, 2016). The subsequent recovery starting around April 26 is likely due to upper densified snow layer enhancing scattering at the air-snow interface rather than within the snowpack (Nandan et al., 2023). These scattering characteristics may also be influenced by snow accumulation through snowfall or redistribution processes. During the early melt phase, backscatter increases steadily across all sites, reaching values of approximately 3–8 dB in association with rising air temperatures. This increase is likely driven by the development of wet snow conditions and associated changes in dielectric properties and surface roughness at the air-snow interface. The timing of this increase coincides with the onset of melt, suggesting that SWOT KaRIn backscatter is sensitive to changes in surface conditions and may capture the transition from cold, dry snow conditions to melt onset.

https://doi.org/10.5194/egusphere-2026-4309
Preprint. Discussion started: 17 August 2026

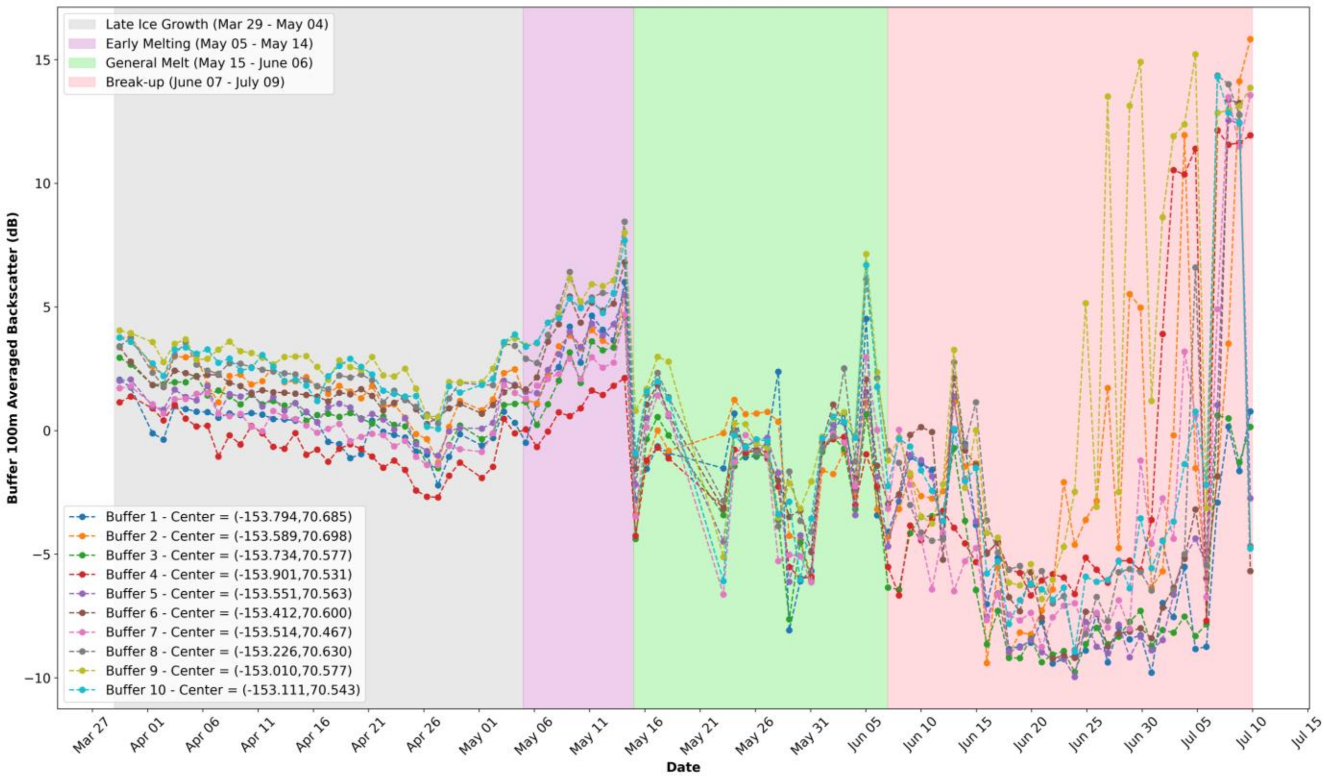

Figure 11: Time series of the SWOT backscatter over Teshekpuk Lake during Cal/Val phase. Shaded areas indicate specific ice phenology events: late ice growth (grey), early melting (purple), general melt (light green), and break-up (light red).

As the early melt season progresses into the general melt phase, the backscatter decreases to below 0 dB and exhibits increased temporal variability, with alternating periods of high and low values across all sites. Nevertheless, the sites display broadly consistent patterns of synchronous increases and decreases, indicating similar surface processes driving the backscatter response. This variability likely indicates intermittent melt and refreeze events, which are common during transitional spring conditions. Daytime warming promotes surface melt, which increases liquid water content and surface roughness, leading to a reduction in backscatter. In contrast, nighttime cooling or short-duration cold spells can induce refreezing, resulting in smoother surface conditions and enhanced backscatter. These fluctuations suggest that SWOT KaRIn backscatter is highly responsive to short-term temperature variations that drive surface state changes during this phase.

During the break-up phase, the backscatter values show significant variability across the different sites. This variability reflects asynchronous melt progression (different regions of the lake become ice-free at different times) as well as the mobility of floating ice. Since the analysis uses a fixed spatial buffer, it repeatedly samples the same geographic location even as ice within

https://doi.org/10.5194/egusphere-2026-4309
Preprint. Discussion started: 17 August 2026

the footprint shifts or is replaced by open water. As the ice retreats and open water appears, the backscatter values increase sharply, often reaching 10–15 dB. The lower backscatter observed on July 05 across all sites, and on July 09 at some sites, is linked to low-wind conditions, as discussed in Section 3.2.2. The spatial differences in the timing of ice melt highlight the complex and heterogeneous nature of the breakup process, which SWOT KaRIn backscatter can effectively capture. Overall, timeseries analysis of the SWOT backscatter reveals its sensitivity to different ice phenology stages, surface roughness, snow metamorphism, surface wetness, melting, and intermittent melt-freeze episodes.

Unlike backscatter, the SWOT KaRIn height time series (Figure 12) shows relatively little variation within each phase. During the first three phases, heights remain nearly constant at around ~1 m above the geoid across all sites, with only small fluctuations and no clear temporal trend. This suggests that, under fully ice-covered conditions, the radar scattering horizon for elevation retrieval is relatively stable, likely occurring at the surface or near-surface of the snowpack. In contrast, the break-up phase shows much higher variability in retrieved heights. This is expected because the lake surface becomes spatially heterogeneous during this period, with a mixture of melting ice, open water, and partially ice-covered areas. In addition, some areas become ice-free earlier than others. As a result, different surface types may dominate the radar return at different locations and times, leading to more variable height estimates. Similar to the backscatter, low-wind conditions (dark-water periods) on July 05 and July 09 also affect SWOT height estimates. However, reasonable height values are observed over Teshekpuk Lake even when surfaces are flagged as dark water in the PIXC product. Such observations should be interpreted cautiously, as this behaviour may not be consistent across all cases. Importantly, the mean water height of Teshekpuk Lake is approximately ~1 m above mean sea level. This baseline corresponds to open water conditions; however, the presence of snow and ice can slightly increase the apparent surface height due to surface accumulation. SWOT height estimates of approximately 1 ± 0.2–0.4 m are consistent with this expected range. The convergence of both open water and ice-covered periods around this value suggests reasonable height retrievals. However, accuracy cannot be commented on with the available information and due to the lack of sufficient in situ surface height measurements.

https://doi.org/10.5194/egusphere-2026-4309
Preprint. Discussion started: 17 August 2026

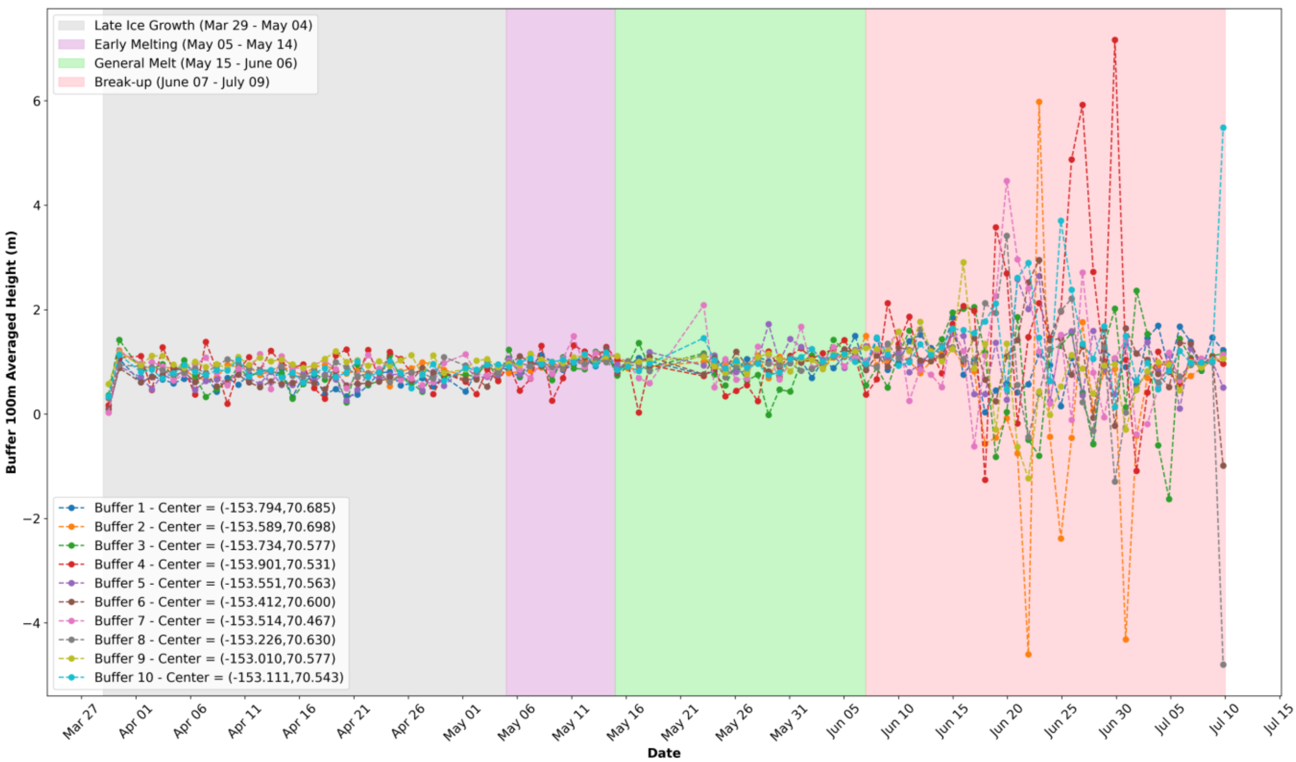

Figure 12: Time series of the SWOT height over Teshekpuk Lake during Cal/Val phase. Shaded areas indicate specific ice phenology events: late ice growth (grey), early melting (purple), general melt (light green), and break-up (light red).

3.3.1 Comparison of SWOT and Field Observations

SWOT-derived heights were evaluated using field observations from Teshekpuk Lake, collected on May 10, 2023, at discrete points along a transect spanning the central basin, as shown in Figure 1 (Jones et al., 2025). To ensure consistency with the in situ observations, SWOT heights are averaged within 30 m buffers around each field campaign transect point (Figure 1). As the field height measurements are referenced to the WGS84 ellipsoid, SWOT heights are also expressed relative to the WGS84 ellipsoid in this section. This differs from the preceding sections, where elevations were referenced to the EGM2008 geoid. Figure 13 shows the comparison between SWOT-derived and field-measured elevations along the transect on Teshekpuk Lake. Overall, the SWOT heights are comparable with field observations, capturing the general spatial pattern of surface elevation across the central basin. This is supported by a strong, statistically significant correlation ($r = 0.89$, $p < 0.001$). At Ka-band frequency, backscatter is primarily sensitive to surface and near-surface snow properties, including grain size, density, and wetness. In the absence of snow cover, it may be influenced by the properties of the exposed ice surface. As expected, SWOT height is slightly lower than the field height in most cases, likely because Ka-band signals penetrate the snowpack and lead to

https://doi.org/10.5194/egusphere-2026-4309
Preprint. Discussion started: 17 August 2026

scattering from within the near-surface layer, or a potential underestimation of surface elevation by SWOT. The deviations may also be due to spatial averaging within the SWOT footprint, temporal mismatch between SWOT overpass and field observation, and additional uncertainties arising from geophysical corrections and field measurements (including surface heterogeneity and potential differences between the measured surface and the true snowpack surface).

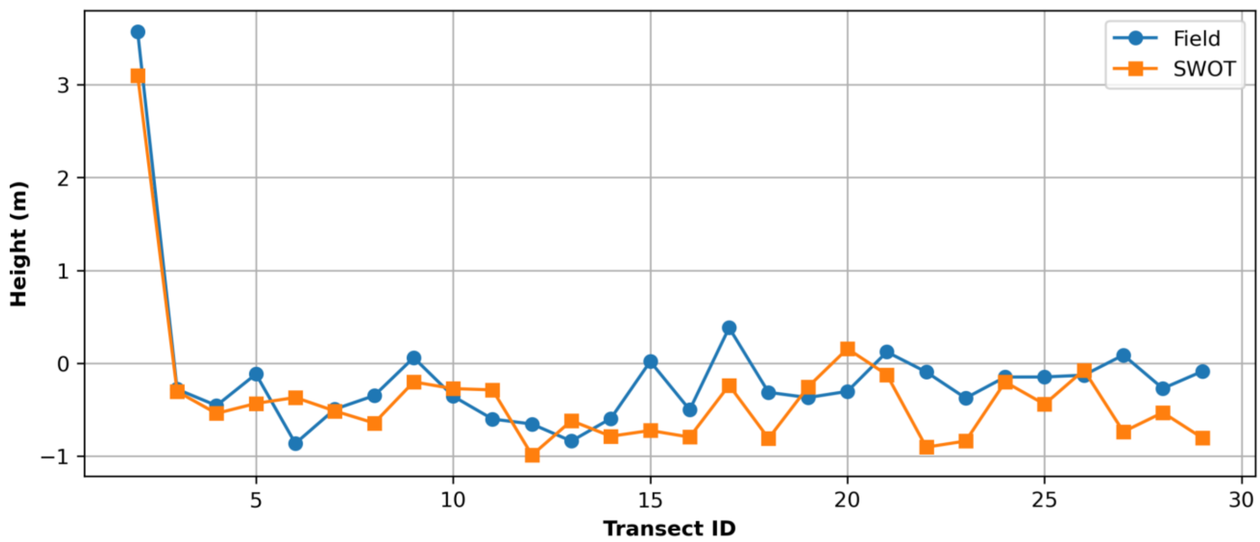

Figure 13: Comparison of SWOT heights and in situ field measurements along a transect across the central basin of Teshekpuk Lake. Field observations were collected during a campaign conducted on May 10, 2023. SWOT heights are averaged within 30 m buffers around corresponding field locations to ensure spatial consistency. All elevations are referenced to the WGS84 ellipsoid.

3.3.2 Simulated SWOT Backscatter and Snow Properties

For further understanding of the impact of snow properties on the observed SWOT backscatter described in the previous sections, a series of simulations was conducted using the snow microwave radiative transfer (SMRT) model (Picard et al., 2018). Simulations were run using a hypothetical snow and ice column as input under cold conditions to support the interpretation of SWOT signals during this period. No simulations were conducted during melt periods. To properly represent conditions over Teshekpuk Lake in mid-March, the average ice thickness of field observations, 1.55 m, was used in SMRT with a temperature of 263.15 K (Jones et al., 2025). The overlying snow layer was represented as two layers. The first layer was simulated as a layer of wind slab (snow density of 293 kg/m^3, snow specific surface area (SSA) of 25.88 m^2 kg^{-1}, and a grain radius of 0.13 mm), and the second layer was simulated as a layer of depth hoar (snow density of 227 kg/m^3, SSA of 10.22 m^2 kg^{-1}, and a grain radius of 0.32 mm). The selected snow properties are based on past observations at Trail Valley Creek in the Northwest Territories, Canada, as well as field observations at Teshekpuk Lake (Rutter et al., 2019; Jones et al., 2025). Snow was parameterized with the sticky hard spheres microstructure model, which uses the snow grain optical radius

https://doi.org/10.5194/egusphere-2026-4309
Preprint. Discussion started: 17 August 2026

determined via SSA. SSA and optical grain size are inversely related; as snow ages, sinters, or melts, the grains become larger and more spherical, resulting in a lower SSA (Braun et al., 2024). SSA is used to calculate optical radius (R_o) via the Eq. (4):

$$R_o = \frac{3}{\rho_{ice} * SSA} \tag{4}$$

where ρ_{ice} is the density of ice set to 916.7 kg m^{-3}. The snow was simulated with the same temperature of 265 K as in past SMRT simulations (Rutter et al., 2019). Roughness was set for three interfaces, air-snow, snow-ice, and ice-water, using the integral equation model (IEM). The air-snow and snow-ice interface were set with a root mean square height of 1 mm and a correlation length of 40 mm. The ice-water interface was set with a root mean square height of 2 mm and a correlation length of 50 mm. To determine how changing snow properties such as snow density, depth, and grain size may impact the SWOT backscatter, the previously mentioned parameters are used as a base. These values are then iterated to evaluate the sensitivity of the backscatter to changes in these properties. Density is varied between 150 and 450 kg m^{-3} at an interval of 5 kg m^{-3} and snow grain radius is varied between 0.05 to 0.5 mm at an interval of 0.001 mm. When one parameter is iterated, other parameters are held constant. Sensitivity experiments are run for different snow depths of 0.1, 0.2, 0.3, 0.4, 0.5 m. SMRT was run using SWOT sensor properties (35.75 GHz frequency and 2.5 ° incidence angle). The results of key simulations are shown in Figure 14.

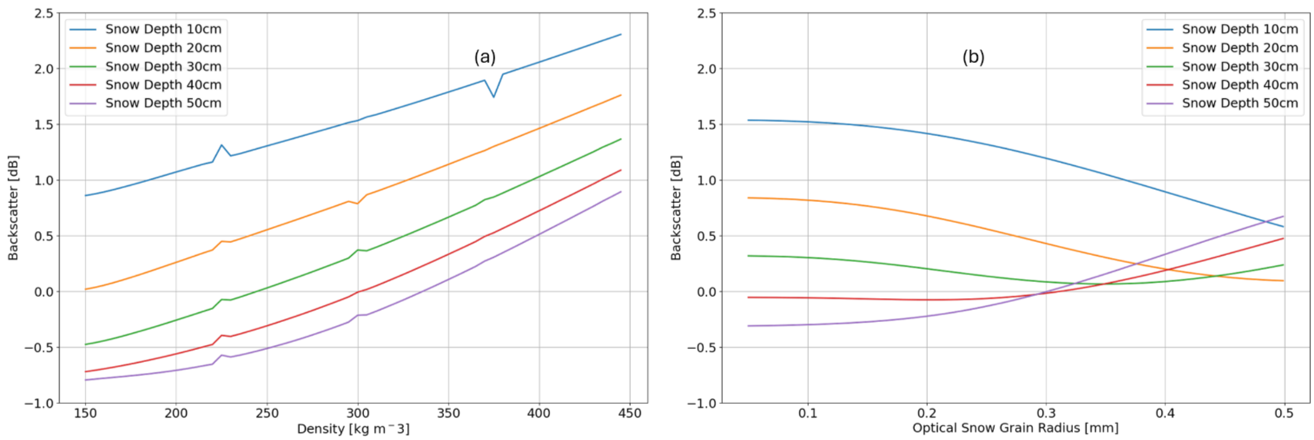

Figure 14: SMRT simulations for a hypothetical 2-layer snowpack with varying snow depth, snow density (a), and grain size (b) for the top layer of snow.

For shallow snow depths, the backscatter decreases from 0.5 to 1 dB. For deeper snow, the increase in backscatter up to 1.5 dB are simulated (Figure 14(b)). The difference between patterns observed in depth is likely due to the interactions that occur

https://doi.org/10.5194/egusphere-2026-4309
Preprint. Discussion started: 17 August 2026

at different layers. Larger grain sizes increase volume scattering and reduce the number of scatters leading to a decrease in backscatter (Krol & Löwe, 2016). However, with the deeper snowpack at 0.3 to 0.5 m, the lower layer can contribute to a higher return resulting in the increase in backscatter (Stroeve et al., 2026). The simulations provide a possible explanation for the upward change in SWOT backscatter starting in late April. When density is increased in the simulations for the top layer of snow, there is also an increase in backscatter (See Figure 14a). This is likely due to an increase in scattering at the air-snow interface (Yueh et al., 2009). The increase in density results in increasing permittivity of the snow layer which will result in more interaction at the air-snow interface and more return of the signal to the sensor as mentioned previously (Nandan et al., 2023; JPL, 2025c). While many past observations are over sea ice (e.g., Nandan et al., 2023), similar physics are expected on Teshekpuk Lake. Increasing density in April–May leading to increases in backscatter could be the result of increasing temperatures, densification, or redistribution of snow. Although limited in scope, the simulations illustrate that a likely connection exists between the evolution in snow properties, which has been documented (Sturm and Benson, 1997; Sturm and Liston, 2003), and SWOT backscatter. The simulations suggest that density and snow depth are the main drivers of the backscatter values. Conducting further simulations, including evaluating the role of increased moisture content, the roughness of different interfaces, and additional exploration of the properties outlined above (snow depth, density, and grain size), is critical for developing inversion models that could leverage SWOT data to retrieve snow properties over lake ice.

4 Conclusions

This study examined the sensitivity of SWOT KaRIn measurements to lake ice and overlying snow over Teshekpuk Lake during the 2023 Cal/Val phase. Analysis of SWOT height and backscatter reveals that both perform well and effectively capture surface elevation (with some limitations) and respond to distinct seasonal patterns likely linked to snow metamorphism, the onset of surface melt, freeze–thaw episodes, and eventual break-up. Because the Cal/Val period only covers from late ice growth to break-up (Mar 29–July 09, 2023), responses during freeze-up and early ice growth could not be assessed. Nevertheless, visual interpretation of SWOT backscatter, alongside optical and SAR imagery and ERA5 temperature data, confirmed that the backscatter signal can identify a range of surface conditions and features, including overlying snow on ice, pressure ridges, inlet streams, surface melting, cracks, fragmented floating ice, and open water. SWOT height estimates are reasonable over open water and ice-covered surfaces before melt onset. However, they are slightly lower than expected values, indicating a small underestimation. In addition, the lack of sufficient in situ observations prevents a full assessment of their accuracy. A notable result is that surfaces flagged as dark water in the product still show physically consistent height and backscatter values; however, caution is required when interpreting these cases, as this behaviour may not be consistent across all instances of the dark-water flag. All these comparisons also highlighted several limitations of SWOT: (1) the specular ringing effect, caused by bright targets near nadir, contaminates surrounding measurements; (2) low or no wind conditions (< 3 m s^{-1}) result in less accurate backscatter and height estimates; (3) the current classification flags need to be improved to better accommodate snow and ice conditions; and (4) height estimates are less reliable over melting snow and ice surfaces.

https://doi.org/10.5194/egusphere-2026-4309
Preprint. Discussion started: 17 August 2026

Despite these limitations, the findings demonstrate the ability of SWOT KaRIn measurements to detect and differentiate various ice phenology events and surface conditions, which are critical for surface type classification. Building on these results, our next study will focus on classifying lake ice types and open water using SWOT data. The outcomes of this work will benefit research on lake water level, lake ice cover, and lake ice thickness estimation from radar altimetry and numerical lake models. In addition, new surface classification flags derived from this study could support the development of correction algorithms tailored to snow and ice conditions, improving the accuracy of height estimates. Given that many northern hemisphere lakes and rivers are seasonally ice-covered, incorporating additional classes for ice and snow in classification maps is essential to ensure reliable data processing and analysis.

Complementary simulations with the SMRT model provided further insight into the SWOT backscatter signal behaviour during the Cal/Val period and reinforced the findings of a likely connection between SWOT backscatter and snow cover properties. The key aspects demonstrated by the simulations are that (1) increasing snow depth results in a decrease in backscatter; (2) larger grain sizes increase volume scatter and result in a decrease in backscatter; and (3) increasing density results in an increase in backscatter. These initial simulations support the connections made within the observed SWOT data that the evolution of the snow (depth, density, SWE, and grain size) is an important consideration in the evolution of SWOT backscatter over lake ice. However, more detailed simulations incorporating additional snow properties, such as moisture content, surface/snowpack wetness and roughness of different interfaces, are needed to better understand KaRIn measurements across different ice phenology stages. Field campaigns focused on snow properties are needed to provide the observations required to support and validate additional simulations investigating the impact of different snow conditions on SWOT signals. Together, these field measurements and simulations are expected to enable the development of robust inversion models for retrieving snow and ice properties from SWOT data and to support the design of algorithms for future satellite missions, including the Copernicus Polar Ice and Snow Topography Altimeter (CRISTAL) and Sentinel-3 Next Generation Topography (S3NG-TOPO).

Data availability

All data used in this study are publicly available. The SWOT Level 2 KaRIn High-Rate Water Mask Pixel Cloud (PIXC), version D, data were obtained from the NASA Physical Oceanography Distributed Active Archive Center (PODAAC; https://doi.org/10.5067/SWOT-PIXC-D). MODIS Aqua and Terra Corrected Reflectance (true-color) imagery was retrieved from NASA Worldview (https://worldview.earthdata.nasa.gov/). Sentinel-2 imagery from the Copernicus Data Space Ecosystem Browser (https://dataspace.copernicus.eu/browser/), and Landsat 8 and 9 imagery from the U.S. Geological Survey (https://earthexplorer.usgs.gov/) were used. Sentinel-1 SAR data were sourced from the Alaska Satellite Facility (https://asf.alaska.edu/) while RADARSAT Constellation Mission (RCM) data were accessed through the Earth Observation Data Management System (EODMS; https://www.eodms-sgdot.nrcan-rncan.gc.ca/index_en.jsp). ERA5-Land hourly 2 m air temperature data were downloaded from the Copernicus Climate Change Service (C3S) Climate Data Store

https://doi.org/10.5194/egusphere-2026-4309
Preprint. Discussion started: 17 August 2026

(https://doi.org/10.24381/cds.e2161bac). ArcticDEM elevation data (version 4.1) were obtained from the Polar Geospatial Center (https://doi.org/10.7910/DVN/3VDC4W). Field data collected for this study are archived at the Arctic Data Center (https://doi.org/10.18739/A21V5BG3V). The SMRT model code is available from https://github.com/smrt-model/smrt/releases#release-v1.3.

Video supplement

Two video animations are provided to visualize the spatiotemporal evolution of SWOT observations over Teshekpuk Lake during the Cal/Val period. Video S1: evolution of SWOT backscatter, height, and ERA5 2 m air temperature (https://doi.org/10.5281/zenodo.21285968, Mugunthan et al., 2026a). Video S2: evolution of the SWOT classification flag (https://doi.org/10.5281/zenodo.21286346, Mugunthan et al., 2026b).

Author contributions

JSM conceptualized the study, developed the methodology, performed data curation, software development, formal analysis, validation, visualization, and prepared the original draft. CRD contributed to conceptualization and supervised the study. JM contributed to data curation, performed SMRT simulations, and prepared the corresponding manuscript section. EZ contributed to interpretation of results. BMJ conducted field data collection and provided contextual knowledge of the study area. JSM, CRD, JM, and EZ contributed to manuscript review and editing. All authors reviewed and approved the final manuscript.

Competing interests

The authors declare that they have no conflict of interest.

Financial support

The authors acknowledge financial support from the Centre national d'études spatiales (CNES), France (ROR: https://ror.org/04h1h0y33), within the framework of the SWOT for Ice-covered Rivers and Lakes (SWIRL), TOSCA project.

https://doi.org/10.5194/egusphere-2026-4309
Preprint. Discussion started: 17 August 2026

References

Alaska Satellite Facility (ASF): NASA ASF Distributed Active Archive Center (DAAC) Vertex interface, https://vertex.daac.asf.alaska.edu/, last access: 07 December 2025.

Armitage, T. W. K. and Kwok, R.: SWOT and the ice-covered polar oceans: An exploratory analysis, Advances in Space Research, 68, 829–842, https://doi.org/10.1016/j.asr.2019.07.006, 2021.

Arp, C. D., Bondurant, A. C., Drew, K. A., and Szatkowski, M. E.: Ice patterns and trends of Teshekpuk Lake: Alaska's longest seasonally ice-covered freshwater system, Arctic Science, 12, 1–17, https://doi.org/10.1139/as-2025-0080, 2026.

Arp, C. D. and Jones, B. M.: The Hydrology and Ice-cover of Teshekpuk Lake in a Changing Arctic Climate, American Water Resources Association 2011 Conference Proceedings, https://ak-awra.org/proceedings/2011abstracts/papers/session1-carp.pdf, 2011.

Arp, C. D., Jones, B. M., and Grosse, G.: Recent lake ice-out phenology within and among lake districts of Alaska, U.S.A, Limnology & Oceanography, 58, 2013–2028, https://doi.org/10.4319/lo.2013.58.6.2013, 2013.

Arp, C. D., Jones, B. M., Schmutz, J. A., Urban, F. E., and Jorgenson, M. T.: Two mechanisms of aquatic and terrestrial habitat change along an Alaskan Arctic coastline, Polar Biol, 33, 1629–1640, https://doi.org/10.1007/s00300-010-0800-5, 2010.

Atwood, D. K., Gunn, G. E., Roussi, C., Wu, J., Duguay, C., and Sarabandi, K.: Microwave Backscatter From Arctic Lake Ice and Polarimetric Implications, IEEE Trans. Geosci. Remote Sensing, 53, 5972–5982, https://doi.org/10.1109/TGRS.2015.2429917, 2015.

Benson, C. S. and Sturm, M.: Structure and wind transport of seasonal snow on the Arctic slope of Alaska, Ann. Glaciol., 18, 261–267, https://doi.org/10.3189/S0260305500011629, 1993.

Biancamaria, S., Lettenmaier, D. P., and Pavelsky, T. M.: The SWOT Mission and Its Capabilities for Land Hydrology, Surv Geophys, 37, 307–337, https://doi.org/10.1007/s10712-015-9346-y, 2016.

Braun, A., Fourteau, K., and Löwe, H.: A rigorous approach to the specific surface area evolution in snow during temperature gradient metamorphism, The Cryosphere, 18, 1653–1668, https://doi.org/10.5194/tc-18-1653-2024, 2024.

Brown, L. C. and Duguay, C. R.: The response and role of ice cover in lake-climate interactions, Progress in Physical Geography: Earth and Environment, 34, 671–704, https://doi.org/10.1177/0309133310375653, 2010.

Duguay, C.R., Bernier, M., Gauthier, Y. and Kouraev, A.: Remote sensing of lake and river ice, Remote sensing of the cryosphere, 273-306, 2015.

European Space Agency (ESA): Copernicus Data Space Ecosystem Browser, https://dataspace.copernicus.eu/browser/, last access: 07 December 2025.

Fayne, J. V. and Smith, L. C.: How Does Wind Influence Near-Nadir and Low-Incidence Ka-Band Radar Backscatter and Coherence from Small Inland Water Bodies?, Remote Sensing, 15, 3361, https://doi.org/10.3390/rs15133361, 2023.

Fischer, R., Farrell, S. L., Duncan, K., and Yi, D.: Swath Mapping Altimetry over Sea Ice: First Results from the Surface Water and Ocean Topography (SWOT) Mission, https://doi.org/10.22541/essoar.174619911.18378288/v1, 2025.

https://doi.org/10.5194/egusphere-2026-4309
Preprint. Discussion started: 17 August 2026

Fjørtoft, R., Gaudin, J.-M., Pourthie, N., Lalaurie, J.-C., Mallet, A., Nouvel, J.-F., Martinot-Lagarde, J., Oriot, H., Borderies, P., Ruiz, C., and Daniel, S.: KaRIn on SWOT: Characteristics of Near-Nadir Ka-Band Interferometric SAR Imagery, IEEE Trans. Geosci. Remote Sensing, 52, 2172–2185, https://doi.org/10.1109/TGRS.2013.2258402, 2014.

Government of Canada: Earth Observation Data Management System (EODMS), https://www.eodms-sgdot.nrcan-rncan.gc.ca/index_en.jsp, last access: 07 December 2025.

Grunblatt, J. and Atwood, D.: Mapping lakes for winter liquid water availability using SAR on the North Slope of Alaska, International Journal of Applied Earth Observation and Geoinformation, 27, 63–69, https://doi.org/10.1016/j.jag.2013.05.006, 2014.

Gunn, G., Duguay, C., Derksen, C., Clausi, D., and Toose, P.: Investigating the Influence of Variable Freshwater Ice Types on Passive and Active Microwave Observations, Remote Sensing, 9, 1242, https://doi.org/10.3390/rs9121242, 2017.

Hall, D. K., Kelly, R. E., Foster, J. L., and Chang, A. T.: Estimation of Snow Extent and Snow Properties, in: Encyclopedia of Hydrological Sciences, edited by: Anderson, M. G. and McDonnell, J. J., Wiley, https://doi.org/10.1002/0470848944.hsa062, 2005.

Howell, S. E. L., Brown, L. C., Kang, K.-K., and Duguay, C. R.: Variability in ice phenology on Great Bear Lake and Great Slave Lake, Northwest Territories, Canada, from SeaWinds/QuikSCAT: 2000–2006, Remote Sensing of Environment, 113, 816–834, https://doi.org/10.1016/j.rse.2008.12.007, 2009.

Jeffries, M.O., Morris, K., and Kozlenko, N.: Ice characteristics and processes, and remote sensing of frozen rivers and lakes, Remote Sensing in Northern Hydrology: measuring environmental change, 163, pp.63-90, https://doi.org/10.1029/GM163, 2005.

Jones, B.M., Kanevskiy, M., Duguay, C., & Mugunthan, J. S.: Surface Elevation, Snow, Ice, and Depth Measurements along a transect at Teshekpuk Lake, Alaska on 10 May 2023, Arctic Data Center, https://doi.org/10.18739/A21V5BG3V, 2025.

Jones, B. M., Rangel, R. C., Parsekian, A. D., Mahoney, A., Kaidel, L., Sformo, T., Wood, J., Husher, C., & Polashenski, C.: Operational viability of Arctic lake ice: Ice growth and runway feasibility at Teshekpuk Lake, Alaska, Journal of Arctic Security, Volume 3, 113–132, 2026.

JPL: SWOT Product Description Document: Level 2 KaRIn High Rate Water Mask Pixel Cloud (L2_HR_PIXC) Data Product, Jet Propulsion Laboratory Internal Document, D-56411, Revision C, 2025a.

JPL: SWOT Project Release Note Version D KaRIn Science Data Products, https://archive.podaac.earthdata.nasa.gov/podaac-ops-cumulus-docs/web-misc/swot_mission_docs/SWOT_VersionD_KaRIn_Products_Release_Note_20250423b.pdf (dated April 23, 2025), 2025b.

JPL: SWOT Science Data Products User Handbook, Jet Propulsion Laboratory Internal Document, D-109532, Revision A, Pasadena, CA, 2025c.

Kacimi, S., Jaruwatanadilok, S., and Kwok, R.: SWOT Observations Over Sea Ice: A First Look, Geophysical Research Letters, 52, e2025GL116079, https://doi.org/10.1029/2025GL116079, 2025.

Kouraev, A., Semovski, S., Shimaraev, M., Mognard, N., Legresy, B., and Remy, F.: Observations of Lake Baikal ice from

https://doi.org/10.5194/egusphere-2026-4309
Preprint. Discussion started: 17 August 2026

satellite altimetry and radiometry, Remote Sensing of Environment, 108, 240–253, https://doi.org/10.1016/j.rse.2006.11.010, 2007.

Kouraev, A. V., Zakharova, E. A., Rémy, F. and Suknev, A. Ya.: Study of lake baikal ice cover from radar altimetry and in–situ observations, Marine Geodesy, 38(sup1), 477–486, doi:10.1080/01490419.2015.1008155, 2015.

Krol, Q. and Löwe, H.: Relating optical and microwave grain metrics of snow: the relevance of grain shape, The Cryosphere, 10, 2847–2863, https://doi.org/10.5194/tc-10-2847-2016, 2016.

Liu, C., Huang, H., Hui, F., Zhang, Z., and Cheng, X.: Fine-Resolution Mapping of Pan-Arctic Lake Ice-Off Phenology Based on Dense Sentinel-2 Time Series Data, Remote Sensing, 13, 2742, https://doi.org/10.3390/rs13142742, 2021.

Mangilli, A., Duguay, C. R., Murfitt, J., Moreau, T., Amraoui, S., Mugunthan, J. S., Thibaut, P., and Donlon, C.: Improving the Estimation of Lake Ice Thickness with High-Resolution Radar Altimetry Data, Remote Sensing, 16, 2510, https://doi.org/10.3390/rs16142510, 2024.

Messager, M. L., Lehner, B., Grill, G., Nedeva, I., and Schmitt, O.: Estimating the volume and age of water stored in global lakes using a geo-statistical approach, Nat Commun, 7, 13603, https://doi.org/10.1038/ncomms13603, 2016.

Mugunthan, J. S.: Evolution of SWOT Height and Backscatter with ERA5 Air Temperature over Teshekpuk Lake during the Cal/Val Period, Zenodo [video], https://doi.org/10.5281/ZENODO.21285968, 10 July 2026a.

Mugunthan, J. S.: Evolution of the SWOT Classification Flag over Teshekpuk Lake during the Cal/Val Period, Zenodo [video], https://doi.org/10.5281/ZENODO.21286346, 10 July 2026b.

Mugunthan, J. S., Duguay, C. R., and Zakharova, E.: Machine learning based classification of lake ice and open water from Sentinel-3 SAR altimetry waveforms, Remote Sensing of Environment, 299, 113891, https://doi.org/10.1016/j.rse.2023.113891, 2023.

Muñoz Sabater, J.: ERA5-Land hourly data from 1950 to present, Copernicus Climate Change Service (C3S) Climate Data Store (CDS) [data set], https://doi.org/10.24381/cds.e2161bac, 2019.

Murfitt, J. and Brown, L. C.: Lake ice and temperature trends for Ontario and Manitoba: 2001 to 2014, Hydrological Processes, 31, 3596–3609, https://doi.org/10.1002/hyp.11295, 2017.

Murfitt, J. and Duguay, C. R.: Assessing the Performance of Methods for Monitoring Ice Phenology of the World's Largest High Arctic Lake Using High-Density Time Series Analysis of Sentinel-1 Data, Remote Sensing, 12, 382, https://doi.org/10.3390/rs12030382, 2020.

Murfitt, J. and Duguay, C. R.: 50 years of lake ice research from active microwave remote sensing: Progress and prospects, Remote Sensing of Environment, 264, 112616, https://doi.org/10.1016/j.rse.2021.112616, 2021.

Nandan, V., Willatt, R., Mallett, R., Stroeve, J., Geldsetzer, T., Scharien, R., Tonboe, R., Yackel, J., Landy, J., Clemens-Sewall, D., Jutila, A., Wagner, D. N., Krampe, D., Huntemann, M., Mahmud, M., Jensen, D., Newman, T., Hendricks, S., Spreen, G., Macfarlane, A., Schneebeli, M., Mead, J., Ricker, R., Gallagher, M., Duguay, C., Raphael, I., Polashenski, C., Tsamados, M., Matero, I., and Hoppmann, M.: Wind redistribution of snow impacts the Ka- and Ku-band radar signatures of Arctic sea ice, The Cryosphere, 17, 2211–2229, https://doi.org/10.5194/tc-17-2211-2023, 2023.

https://doi.org/10.5194/egusphere-2026-4309
Preprint. Discussion started: 17 August 2026

National Aeronautics and Space Administration (NASA): Worldview, https://worldview.earthdata.nasa.gov/, last access: 07 December 2025.

Picard, G., Sandells, M., and Löwe, H.: SMRT: an active–passive microwave radiative transfer model for snow with multiple microstructure and scattering formulations (v1.0), Geosci. Model Dev., 11, 2763–2788, https://doi.org/10.5194/gmd-11-2763-2018, 2018.

Porter, C., Howat, I., Noh, M.-J., Husby, E., Khuvis, S., Danish, E., Tomko, K., Gardiner, J., Negrete, A., Yadav, B., Klassen, J., Kelleher, C., Cloutier, M., Bakker, J., Enos, J., Arnold, G., Bauer, G., and Morin, P.: ArcticDEM - Mosaics, Version 4.1, https://doi.org/10.7910/DVN/3VDC4W, 2023.

Prowse, T., Alfredsen, K., Beltaos, S., Bonsal, B., Duguay, C., Korhola, A., McNamara, J., Vincent, W. F., Vuglinsky, V., and Weyhenmeyer, G. A.: Arctic Freshwater Ice and Its Climatic Role, AMBIO, 40, 46–52, https://doi.org/10.1007/s13280-011-0214-9, 2011.

Rangel, R. C., Jones, B. M., Parsekian, A. D., Mahoney, A., Jones, M. W., Sformo, T., Person, B., and George (in Dedication), C.: Annual dynamics of Arctic lake ice pressure ridge formation in Teshekpuk Lake, Alaska, EGU General Assembly 2025, Vienna, Austria, 27 Apr–2 May 2025, EGU25-13480, https://doi.org/10.5194/egusphere-egu25-13480, 2025.

Rodríguez-Morales, F., Li, J., Alvestegui, D. G.-G., Shang, J., Arnold, E. J., Leuschen, C. J., Larsen, C. F., Shepherd, A., Hvidegaard, S. M., and Forsberg, R.: A Compact, Reconfigurable, Multi-UWB Radar for Snow Thickness Evaluation and Altimetry: Development and Field Trials, IEEE J. Sel. Top. Appl. Earth Observations Remote Sensing, 14, 6755–6765, https://doi.org/10.1109/JSTARS.2021.3092313, 2021.

Rutter, N., Sandells, M. J., Derksen, C., King, J., Toose, P., Wake, L., Watts, T., Essery, R., Roy, A., Royer, A., Marsh, P., Larsen, C., and Sturm, M.: Effect of snow microstructure variability on Ku-band radar snow water equivalent retrievals, The Cryosphere, 13, 3045–3059, https://doi.org/10.5194/tc-13-3045-2019, 2019.

Stroeve, J., Nandan, V., Willatt, R., Tonboe, R., Hendricks, S., Ricker, R., Mead, J., Mallett, R., Huntemann, M., Itkin, P., Schneebeli, M., Krampe, D., Spreen, G., Wilkinson, J., Matero, I., Hoppmann, M., and Tsamados, M.: Surface-based Ku- and Ka-band polarimetric radar for sea ice studies, The Cryosphere, 14, 4405–4426, https://doi.org/10.5194/tc-14-4405-2020, 2020.

Stroeve, J., Willatt, R., Downie, M., Saha, M., Nab, C., Fallows, A., Soriot, C., Mallett, R., Komarov, A., Nandan, V., Newman, T., and Yackel, J.: Mapping Snow on Northern Winter Roads: A Dual-Frequency Polarimetric Radar Approach for Snow Characterization over Land, Lake and Sea ice, https://doi.org/10.5194/egusphere-2026-212, 10 February 2026.

Sturm, M. and Benson, C. S.: Vapor transport, grain growth and depth-hoar development in the subarctic snow, J. Glaciol., 43, 42–59, https://doi.org/10.3189/S0022143000002793, 1997.

Sturm, M. and Liston, G. E.: The snow cover on lakes of the Arctic Coastal Plain of Alaska, U.S.A., J. Glaciol., 49, 370–380, https://doi.org/10.3189/172756503781830539, 2003.

Surface Water Ocean Topography (SWOT): SWOT Level 2 Water Mask Pixel Cloud Data Product, Version D. Ver. D. PO.DAAC, CA, USA. Dataset accessed [2025-12-07] at https://doi.org/10.5067/SWOT-PIXC-D, 2025.

https://doi.org/10.5194/egusphere-2026-4309
Preprint. Discussion started: 17 August 2026

Trudel, M., Gribi, T., Siles, G., Biancamaria, S., and Fjørtoft, R.: Impact of Ice, Snow, Wind, and Rain on Swot Water Detection over Canadian Lakes During Cal/Val, in: IGARSS 2024 - 2024 IEEE International Geoscience and Remote Sensing Symposium, 3180–3183, https://doi.org/10.1109/IGARSS53475.2024.10641139, 2024.

Ulaby, F. T., Moore, R. K., and Fung, A. K.: Microwave remote sensing: Active and passive, Volume 2: Radiometry theory and scattering models, Artech House, 1986.

U.S. Geological Survey (USGS): EarthExplorer, https://earthexplorer.usgs.gov/, last access: 07 December 2025.

Verpoorter, C., Kutser, T., Seekell, D. A., and Tranvik, L. J.: A global inventory of lakes based on high-resolution satellite imagery, Geophys. Res. Lett., 41, 6396–6402, https://doi.org/10.1002/2014GL060641, 2014.

Verron, J., Bonnefond, P., Andersen, O., Ardhuin, F., Bergé-Nguyen, M., Bhowmick, S., Blumstein, D., Boy, F., Brodeau, L., Crétaux, J.-F., Dabat, M. L., Dibarboure, G., Fleury, S., Garnier, F., Gourdeau, L., Marks, K., Queruel, N., Sandwell, D., Smith, W. H. F. and Zaron, E. D.: The SARAL/Altika Mission: A step forward to the future of Altimetry, Advances in Space Research, 68(2), 808–828, doi:10.1016/j.asr.2020.01.030, 2021.

Wang, X., Feng, L., Gibson, L., Qi, W., Liu, J., Zheng, Y., Tang, J., Zeng, Z., and Zheng, C.: High-Resolution Mapping of Ice Cover Changes in Over 33,000 Lakes Across the North Temperate Zone, Geophysical Research Letters, 48, e2021GL095614, https://doi.org/10.1029/2021GL095614, 2021.

Yueh, S. H., Dinardo, S. J., Akgiray, A., West, R., Cline, D. W., and Elder, K.: Airborne Ku-Band Polarimetric Radar Remote Sensing of Terrestrial Snow Cover, IEEE Transactions on Geoscience and Remote Sensing, 47, 3347–3364, https://doi.org/10.1109/TGRS.2009.2022945, 2009.

Zemp, M., Chao, Q., Han Dolman, A. J., Herold, M., Krug, T., Speich, S., Suda, K., Thorne, P., and Yu, W.: GCOS 2022 Implementation Plan, 244, 85, https://doi.org/10.5167/uzh-224271, 2022.